

THE GIANT, HORIZONTAL AND ASYMPTOTIC BRANCHES OF GALACTIC GLOBULAR CLUSTERS. I. THE CATALOG, PHOTOMETRIC OBSERVABLES AND FEATURES

F.R. Ferraro^{1,2}, M. Messineo², F. Fusi Pecci^{2,3}, M.A. De Palo⁴,
O. Straniero⁵, A. Chieffi⁶, M. Limongi⁷

ABSTRACT

A catalog including a set of the most recent Color Magnitude Diagrams (CMDs) is presented for a sample of 61 Galactic Globular Clusters (GGCs). We used this data-base to perform an homogeneous systematic analysis of the evolved sequences (namely, Red Giant Branch (RGB), Horizontal Branch (HB) and Asymptotic Giant Branch (AGB)). Based on this analysis, we present: (1) a new procedure to measure the level of the *ZAHB* (V_{ZAHB}) and an homogeneous set of distance moduli obtained adopting the HB as *standard candle*; (2) an independent estimate for RGB metallicity indicators and new calibrations of these parameters in terms of both spectroscopic ($[\text{Fe}/\text{H}]_{\text{CG97}}$) and global metallicity ($[\text{M}/\text{H}]$, including also the α -elements enhancement). The set of equations presented can be used to simultaneously derive a *photometric* estimate of the metal abundance and the reddening from the morphology and the location of the RGB in the $(V, B - V)$ -CMD. (3) the location of the RGB-Bump (in 47 GGCs) and the AGB-Bump (in 9 GGCs). The dependence of these features on the metallicity is discussed. We find that by using the latest theoretical models and the new metallicity scales the earlier discrepancy between theory and observations (~ 0.4 mag) completely disappears.

Subject headings: globular clusters – stars: Population II – stars: Red Giants – stars: Horizontal Branch – stars: evolution

¹European Southern Observatory, Karl Schwarzschild Strasse, 2, D-85748 Garching bei Munchen, GERMANY

²on leave from Osservatorio Astronomico di Bologna, via Zamboni 33, I-40126 Bologna, ITALY

³Stazione Astronomica di Cagliari, 09012 Capoterra, ITALY

⁴Dipartimento di Astronomia, Università di Bologna, I-40126 Bologna, ITALY

⁵Osservatorio Astronomico di Collurania, via M. Vaggini, I-64100 Teramo, ITALY

⁶Istituto di Astrofisica Spaziale del CNR, CP 67, I-00044 Frascati, ITALY

⁷Osservatorio Astronomico di Monte Porzio, I-00040 Monte Porzio Catone, Italy

1. Introduction

Stellar evolutionary models are often used to infer relevant properties of the Galaxy and the early Universe; for this reason the check of their adequacy and accuracy can be regarded as a *pivotal* project of the modern astrophysical research (Renzini & Fusi Pecci 1988).

The advent of the charge-coupled device (CCD) and, more recently, the availability of the *Hubble Space Telescope*, supported by the modern highly powerful software for photometric data analysis in crowded fields, have greatly enhanced the possibility of using the Galactic Globular Clusters (GGCs) as the ideal laboratory to test the stellar evolution theories.

Within this framework, we started a long term project devoted to carry out a detailed quantitative analysis of the evolved sequences (namely, Red Giant Branch, Horizontal Branch, Asymptotic Giant Branch, hereafter RGB, HB, AGB, respectively) in the Colour Magnitude Diagram (CMD) of GGCs.

The methodological approach of our study has been presented in a series of papers concerning the photometry of wide samples of stars in a selected set of GGCs (see for example Ferraro et al. 1990, 1991, 1992a,b, 1993, 1994, 1995, 1997a and Buonanno et al. 1994). Some results on specific sequences can be found in Fusi Pecci et al. 1990 (hereafter F90) and Ferraro 1992 (for the RGB), Fusi Pecci et al. 1992, 1993, Buonanno et al 1997, Ferraro 1997b, 1998a (for the HB), Ferraro, Bellazzini & Fusi Pecci, 1995, Ferraro et al. 1993b, 1997c, 1998b (for the Blue Stragglers).

This is the first in a series of papers devoted to study the characteristics of the RGB, HB and AGB for the widest available sample of GGCs with *good BV* photometry. In this paper we present the catalog of the most recent CMDs for GGCs. From these we derive photometric observables along RGB, HB, and AGB which yield new independent measures of some peculiar features (e.g., the so-called RGB Bump). The study will soon be extended in a second paper to explore the existence and extent of mixing processes (like the semiconvection and overshooting) in the stellar interiors. These processes have a *direct* impact on the duration of the post helium-flash phases (HB and AGB) and, in turn, on the use of population ratios to determine one of the fundamental cosmological parameters, the helium abundance (Y_p), via the so-called *R-method* (Iben 1968, Buzzoni et al 1983).

The paper is organized as follows: in Section 2, we present the complete data-base used in our analysis, which includes CMDs for 61 GGCs; while Section 3 is devoted to the discussion of the metallicity scales. Section 4 reports the basic assumptions of the theoretical models adopted all along the paper. In Section 5, we present a new procedure (based on the use of synthetic CMDs) to measure the level of the Zero-Age HB (frequently adopted as *standard luminosity reference*). Section 6 deals with the presentation of new homogenous determinations of the RGB morphologic parameters, their calibrations in terms of the adopted spectroscopic and global metallicities, and the determination of the RGB-Bump luminosity and its comparison with the theoretical expectations. Similarly, Section 7 is devoted to the study of the photometric properties of the AGB-Bump. Finally, in Section 8, after adopting different self-consistent distance scales, we report the results of a global comparisons with the absolute quantities predicted by the theoretical models.

2. THE DATABASE

After reviewing the published literature on CMDs for GGCs, it is a little surprising to discover that the number of GGCs for which a modern (CCD) CMD is available is less than 50% of the whole cluster population in the Galaxy. This percentage is further decreased if one restricts the sample, as we did, to only the clusters with CMDs of sufficient photometric accuracy, population size, and degree of completeness down the HB blue extension.

Moreover, since we want to perform homogenous independent measures and star counts over the whole CMD, we included in our final sample only the GGCs whose data-sets (star magnitudes and positions) were available on electronic files (upon direct request to the author or scanned from the reference paper). In the final choice, we dropped CMDs with inadequate completeness checks and usually adopted the most recent papers. If different CMDs of comparable quality were available for the same cluster, after carefully checking the radial extension of the samples and their photometric compatibility, we merged them in order to increase the statistical significance of the adopted sample.

The final sample of GGCs whose CMDs have been classified as “good enough” includes 61 objects, for which we list in Table 1: the name, the metallicity in the considered scales (see next section), the reddening from a recent compilation (Harris, 1996), and the reference of the adopted CMD.

Admittedly, the selected sample (listed in Table 1) is quite heterogeneous in many respect: the cluster light sampling, the photometric accuracy and the absolute calibration actually achieved by each individual photometry. However, no attempt has been performed at this level to rank the clusters on the basis of the overall quality of the CMD. In the next paper, specifically devoted to presentation and discussion of the population ratios, a more significative classification will be performed on the basis of the global population of bright stars (AGB + HB + RGB) sampled in each cluster.

3. METALLICITY SCALES

3.1. The Zinn scale

One of the most widely used scales for the metal abundance in GGCs has been proposed during the early 80's by Zinn and his collaborators (Zinn 1980, Zinn & West 1984, Zinn 1985, hereafter Z85, and Armandroff & Zinn 1988). This scale was obtained from the integrated light parameter Q_{39} tied to the Cohen (1983) high dispersion and low resolution spectrograms (see Zinn & West 1984). Though dated, this metallicity scale is still the most complete (121 GGCs) and homogeneous data-base available in the literature. In the following, we will label as Z85 the metallicity values listed in column 4 of Table IV by Armandroff and Zinn (1988) or in column 2 of Table I by Zinn (1985).

3.2. The Carretta and Gratton scale

Recently, Carretta & Gratton (1997, hereafter CG97) have presented new measures of chemical abundances using high dispersion spectra for a set of 24 GGCs, in the metallicity range ($-2.24 < [\text{Fe}/\text{H}]_{\text{Z85}} < -0.54$). Though based on a small number of giants (the total sample includes ~ 160 stars, and in many cases only a few giants have been measured in each cluster), these measures have the advantage of measuring *directly* the equivalent widths of Fe I and Fe II lines. Comparing their new abundances to the Z85 metallicities, CG97 concluded that the Z85 scale is not linear and gave a quadratic relation suitable to transform the Z85 scale to their own scale (see eq. 7 in CG97).

As emphasized by CG97, the transformation relation can be safely used only in the metallicity range $-2.24 < [\text{Fe}/\text{H}]_{\text{Z85}} < -0.54$. In general, the CG97 scale turns out to yield higher metallicity ($\delta[\text{Fe}/\text{H}] \sim 0.2$) with respect to the Z85 scale for low-intermediate metallicity GGCs and lower abundances ($\delta[\text{Fe}/\text{H}] \sim 0.1$) for metal rich GGCs.

For the sample of GGCs listed in Table 1 we eventually adopted the metallicity in the CG97 scale ($[\text{Fe}/\text{H}]_{\text{CG97}}$) with the following assumptions:

1. 20 GGCs have direct spectroscopic measures in CG97. For these clusters the value listed in Table 8 by CG97 has been adopted.
2. 35 GGCs in the quoted range of metallicity ($-2.24 < [\text{Fe}/\text{H}]_{\text{Z85}} < -0.54$) have metallicities only in Z85. For them, we computed the $[\text{Fe}/\text{H}]_{\text{CG97}}$ using eq. 7 of CG97.
3. 6 GGCs in our catalog (namely, NGC 5053, 5927, 6440, 6528, 6553, and Ter 7) have Z85 values outside the validity range of the transformation to the CG97 scale. For these objects we adopted $[\text{Fe}/\text{H}]_{\text{CG97}} = [\text{Fe}/\text{H}]_{\text{Z85}} + \delta[\text{Fe}/\text{H}]_{-0.54}$ and $[\text{Fe}/\text{H}]_{\text{CG97}} = [\text{Fe}/\text{H}]_{\text{Z85}} + \delta[\text{Fe}/\text{H}]_{-2.24}$ for clusters with $[\text{Fe}/\text{H}]_{\text{Z85}} > -0.54$ and $[\text{Fe}/\text{H}]_{\text{Z85}} < -2.24$, respectively. Where $\delta[\text{Fe}/\text{H}]_{-0.54}$ and $\delta[\text{Fe}/\text{H}]_{-2.24}$ are the corrections, computed via eq. 7 by CG97, at $[\text{Fe}/\text{H}]_{\text{Z85}} = -0.54$ and -2.24 , respectively.

3.3. Comparison with another recent catalog

Recently Rutledge, Hesser & Stetson (1997, hereafter RHS97) used homogeneous observations of the CaII triplet lines in a sample of 71 GGCs in order to measure an *abundance index* which should provide a relatively accurate metallicity ranking. RHS97 calibrated this index in both the Zinn and CG97 metallicity scales. Figure 1a,b shows the residuals between the metallicities by RHS97 (in their Table 2) in the Z85 and CG97 scales, respectively, and the values assumed in this paper for the 42 clusters in common. As can be seen from both the panels, most of the clusters are lying within ± 0.2 dex (which is a conservative but still reliable level of the global accuracy for metal abundance determinations for GGCs). From Figure 1a,b it is evident that the residuals do not show any trend with respect to the metallicity. Only a few clusters (namely NGC5053, NGC6366 and Ter7 in Fig1a and NGC5053 in Fig1b, respectively), show a larger ($\delta[\text{Fe}/\text{H}] > 0.4$) scatter and deserve a more accurate spectroscopic analysis.

Table 1. The adopted data-base

<i>Name</i>	[Fe/H] _{Z85}	[Fe/H] _{CG97}	[M/H]	$E(B - V)$	<i>Reference</i>
NGC 104	-0.71	-0.70	-0.59	0.04	Montegriffo et al.(1995) + Hesser et al (1987)
NGC 288	-1.40	-1.07	-0.85	0.03	Bergbush (1993)+ Buonanno et al (1984)
NGC 362	-1.28	-1.15	-0.99	0.05	Harris (1982)
NGC1261	-1.31	-1.09	-0.89	0.02	Ferraro et al. (1993a)
NGC1466	-1.85	-1.64	-1.44	0.09	Walker (1992a)
NGC1841	-2.20	-2.11	-1.91	0.18	Walker (1990)
NGC1851	-1.29	-1.08	-0.88	0.02	Walker (1992b)
NGC1904	-1.69	-1.37	-1.22	0.01	Ferraro et al. (1992)
NGC2419	-2.10	-1.97	-1.77	0.03	Christian et al. (1988)
NGC2808	-1.37	-1.15	-0.95	0.23	Ferraro et al. (1990)
NGC3201	-1.61	-1.23	-1.03	0.21	Covino et al. (1997)
NGC4147	-1.80	-1.58	-1.38	0.02	Sandage & Walker (1955)
NGC4372	-2.08	-1.94	-1.74	0.45	Brocato et al. (1996)
NGC4590	-2.09	-1.99	-1.81	0.04	Walker (1994)
NGC4833	-1.86	-1.58	-1.27	0.33	Momany (1996)
NGC5053	-2.58	-2.51	-2.31	0.03	Sarajedini & Milone (1995)
NGC5272	-1.66	-1.34	-1.16	0.01	Buonanno et al 1994+ Ferraro et al. (1997)
NGC5286	-1.79	-1.57	-1.37	0.24	Brocato et al. (1996)
NGC5466	-2.22	-2.14	-1.94	0.00	Buonanno, Corsi & Fusi Pecci (1985)
NGC5694	-1.91	-1.72	-1.52	0.09	Ortolani & Gratton (1990)
NGC5824	-1.85	-1.64	-1.44	0.14	Bocato et al. (1996)
NGC5897	-1.68	-1.59	-1.44	0.08	Ferraro, Fusi Pecci & Buonanno (1992)
NGC5904	-1.40	-1.11	-0.90	0.03	Buonanno et al. (1981)+ Brocato et al. (1995)
NGC5927	-0.31	-0.46	-0.37	0.47	Samus et al. (1996)
NGC6093	-1.64	-1.41	-1.21	0.18	Brocato et al (1998)
NGC6121	-1.33	-1.19	-0.94	0.36	Lee (1977)
NGC6171	-0.99	-0.87	-0.70	0.33	Ferraro et al. (1991)
NGC6205	-1.65	-1.39	-1.18	0.02	Paltrinieri et al. (1998)
NGC6218	-1.61	-1.37	-1.17	0.17	Brocato et al. (1996)
NGC6229	-1.54	-1.30	-1.10	0.01	Carney, Fullton, Trammell (1991)+ Borissova et al.(1997)
NGC6254	-1.60	-1.41	-1.25	0.28	Harris, Racine ,De Roux (1976)
NGC6266	-1.28	-1.07	-0.87	0.47	Brocato et al. (1996)
NGC6333	-1.78	-1.56	-1.36	0.36	Janes & Heasley (1991)
NGC6341	-2.24	-2.16	-1.95	0.02	Buonanno, Corsi & Fusi Pecci (1985)
NGC6352	-0.51	-0.64	-0.50	0.21	Bordoni (1995)
NGC6366	-0.99	-0.87	-0.70	0.69	Pike (1976)
NGC6397	-1.91	-1.82	-1.65	0.18	Kaluzny (1997)
NGC6440	-0.34	-0.49	-0.40	1.09	Ortolani et al. (1994a)
NGC6528	-0.23	-0.38	-0.31	0.62	Ortolani et al. (1995)
NGC6535	-1.75	-1.53	-1.33	0.32	Sarajedini (1994a)

Table 1—Continued

<i>Name</i>	$[\text{Fe}/\text{H}]_{\text{Z85}}$	$[\text{Fe}/\text{H}]_{\text{CG97}}$	$[\text{M}/\text{H}]$	$E(B - V)$	<i>Reference</i>
NGC6553	-0.29	-0.44	-0.36	0.84	Ortolani et al. (1995)
NGC6584	-1.54	-1.30	-1.10	0.11	Sarajedini & Forrester (1995)
NGC6637	-0.59	-0.68	-0.55	0.17	Ferraro et al. (1994)
NGC6652	-0.99	-0.87	-0.70	0.09	Ortolani et al. (1994b)
NGC6681	-1.51	-1.27	-1.07	0.07	Brocato et al. (1996)
NGC6712	-1.01	-0.88	-0.71	0.46	Cudworth (1988)
NGC6717	-1.32	-1.10	-0.90	0.21	Brocato et al. (1996)
NGC6752	-1.54	-1.42	-1.21	0.04	Buonanno et al. (1986)
NGC6809	-1.82	-1.61	-1.41	0.07	Desidera (1996)
NGC6838	-0.58	-0.70	-0.49	0.25	Cudworth (1995)
NGC6934	-1.54	-1.30	-1.10	0.11	Brocato et al. (1996)
NGC6981	-1.54	-1.30	-1.10	0.05	Brocato et al. (1996)
NGC7006	-1.59	-1.35	-1.15	0.05	Buonanno et al. (1991)
NGC7078	-2.17	-2.12	-1.91	0.09	Buonanno, Corsi & Fusi Pecci (1985)
NGC7099	-2.13	-1.91	-1.71	0.03	Bergbusch (1996)
NGC7492	-1.51	-1.27	-1.07	0.00	Buonanno et al. (1987)
IC 4499	-1.50	-1.26	-1.06	0.24	Ferraro et al. (1995)
Rup 106	-1.90	-1.70	-1.50	0.21	Buonanno et al. (1993)
Arp 2	-1.85	-1.64	-1.44	0.11	Buonanno et al. (1995a)
Ter 7	-0.49	-0.64	-0.52	0.06	Buonanno et al. (1995b)
Ter 8	-1.81	-1.60	-1.40	0.14	Ortolani & Gratton (1990)

These considerations strongly suggest that the two sets of measurements are fully consistent within the global assumed uncertainty. In order to use the entire GGC data-set we collected, in the following discussion we adopt the metallicity values (in the Zinn and CG97 scales) listed in Table 1. However, for sake of completeness, in Section 9 we further discuss the effect of adopting the metallicity measurements listed by RHS97 instead of those listed in Table 1.

3.4. The global metallicity

In the last decade it has become evident that in Population II stars the abundance of α -elements is enhanced with respect to iron. Direct measurements of the α -elements abundance in the halo field stars have shown a very well defined behaviour as a function of $[\text{Fe}/\text{H}]$, with a nearly constant overabundance ($[\alpha/\text{Fe}] \sim 0.4$) for $[\text{Fe}/\text{H}] < -2$ and a well defined trend with metallicity, which linearly decreases to $[\alpha/\text{Fe}] \sim 0.0$ as metallicity increases (see Edvardsson et al 1993, Nissen et al 1994, Magain 1989, Zhao & Magain 1990, Gratton et al 1996). In the GGC system the situation is not so clear. The mean overabundance seems to be $[\alpha/\text{Fe}] \sim 0.3$, but the behaviour with respect to the metallicity is still not firmly established. For example Carney (1996) claims that α -element

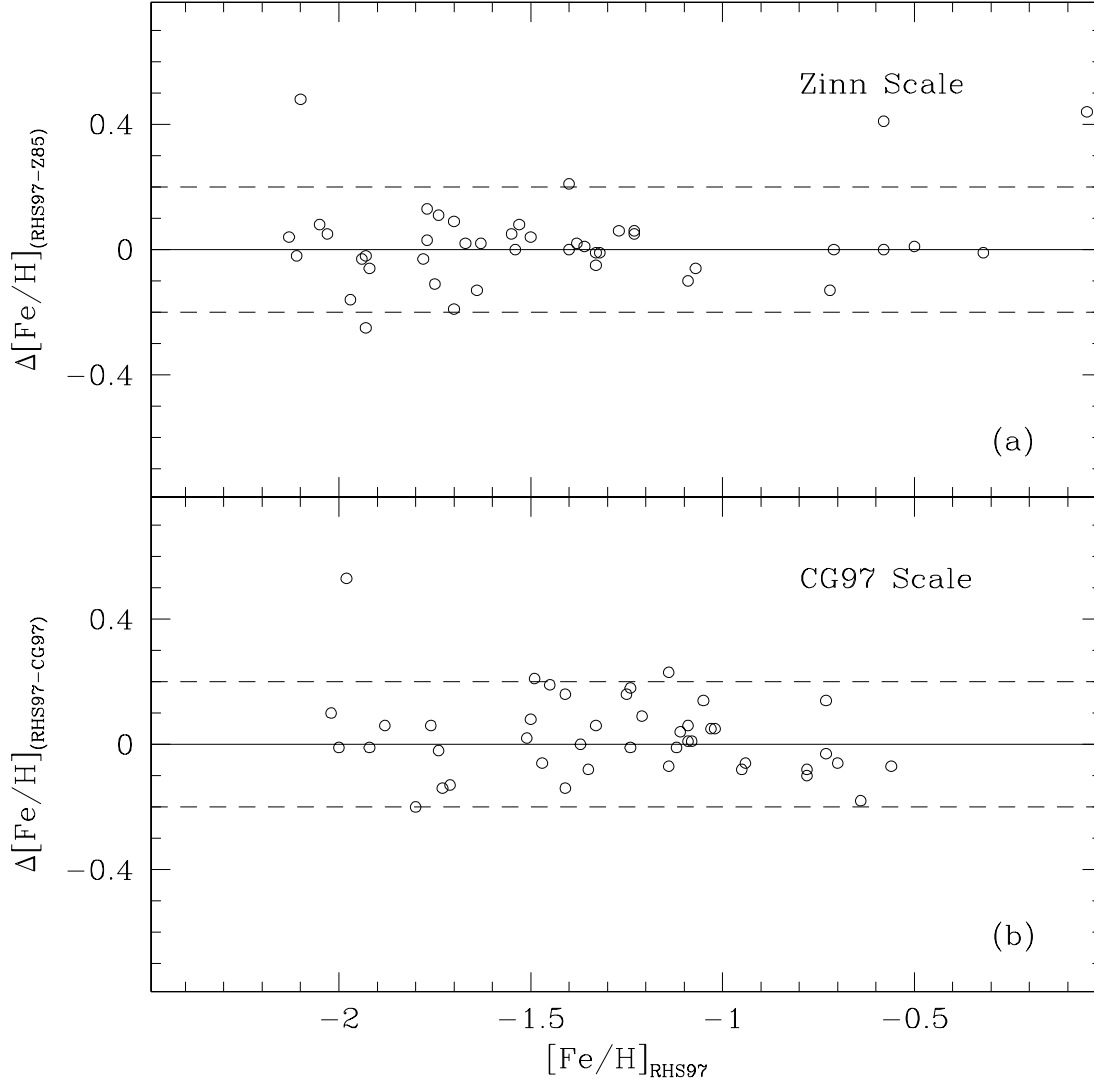


Fig. 1.— Residuals between metallicities by RHS97 (listed in their Table 2) in the Zinn [*panel (a)*] and in the CG97 scale [*panel (b)*], respectively, and the values assumed in this paper (see Table 1) for the 42 clusters in common.

abundances do not appear to vary as a function of $[\text{Fe}/\text{H}]$ in GGCs.

There are two recent compilations listing the α -element abundances measured in GGCs: Carney (1996) and Salaris & Cassisi (1996). Especially in the second list the data are collected from different sources and are not the result of independent, self-consistent observations. However, they can be used to have useful quantitative hints.

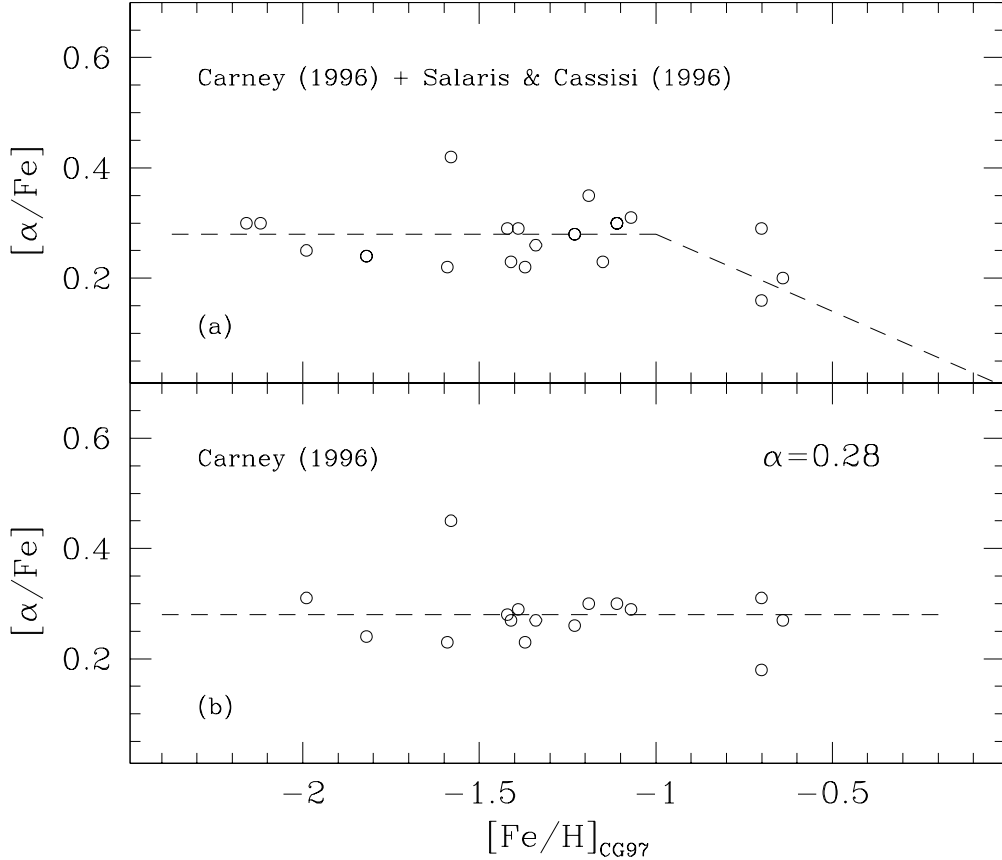


Fig. 2.— $[\alpha/Fe]$ as a function of $[Fe/H]_{CG97}$. *Panel (a)*: $[\alpha/Fe]$ are from Salaris & Cassisi (1996) and Carney (1996). For the 16 objects in common in the two lists the $[\alpha/Fe]$ values have been averaged. The dashed line is the *enhancement-relation* as a function of the metallicity which we assumed all along the paper. *Panel (b)*: $[\alpha/Fe]$ measures are from Carney (1996). The dashed line represents the scenario suggested by Carney (1996) for a constant *enhancement* with varying the metallicity.

In our catalog 16 GGCs have values listed in Table 2 by Carney (1996), and 19 in Table 1 by Salaris & Cassisi (1996). There are 16 objects in common in the two lists, and the values are in fairly good agreement (within 0.15 dex). In the following, we will adopt for $[\alpha/Fe]$ the average of the values listed in the two tables. Figure 2a shows $[\alpha/Fe]$ as a function of the metallicity in the CG97 scale. Admittedly, it is hard to define a clear-cut trend with metallicity. However, the $[\alpha/Fe]$ abundance for $[Fe/H]_{CG97} < -1$ is compatible with a constant plateau, and for these clusters a

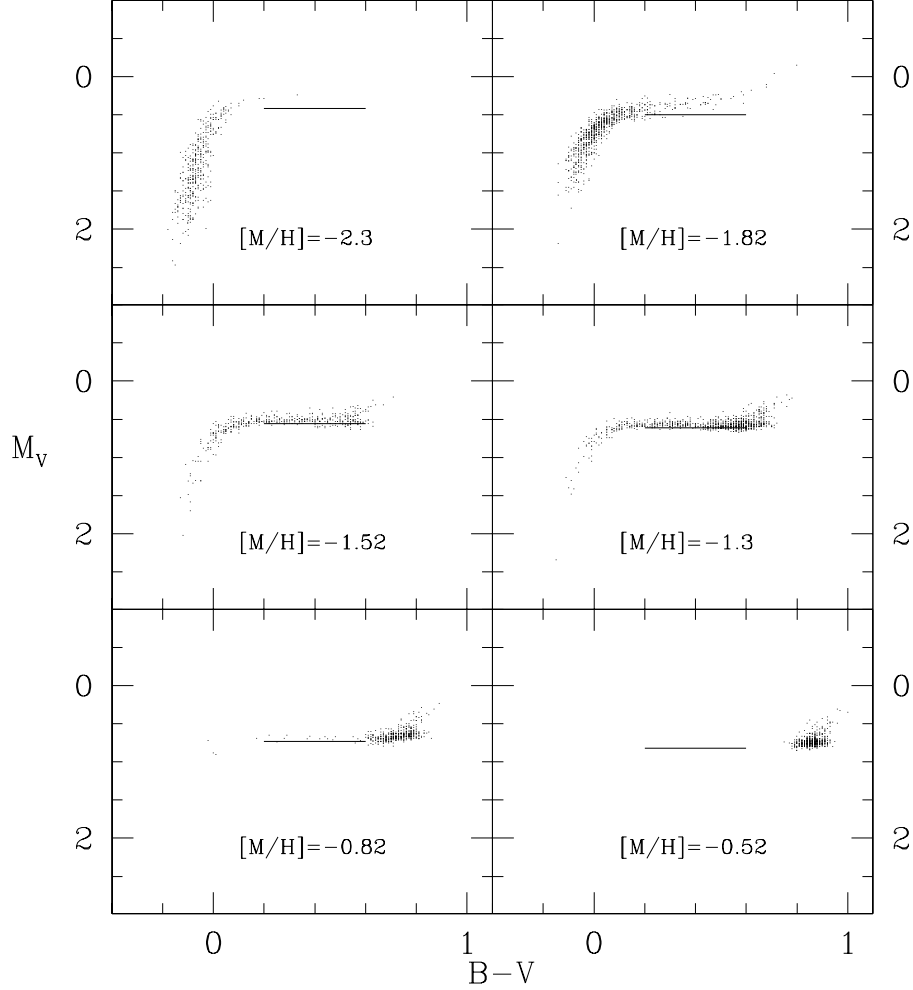


Fig. 3.— Synthetic HB at different metallicities. The ZAHB level at $\log T_{\text{eff}} = 3.85$ is plotted as solid line.

mean value of $[\alpha/\text{Fe}] = 0.28$ has been adopted. At the metal rich extreme the situation is less clear. There are only 3 clusters with $[\text{Fe}/\text{H}]_{\text{CG97}} > -1$. The dashed line in Figure 2a shows that their α -element abundances are consistent with a linear decrease with increasing metallicity similar to that seen in the field stars. For sake of simplicity, in the following we have thus adopted such a trend for the metal rich GGCs. However since the global trend of $[\alpha/\text{Fe}]$ with metallicity is still not firmly established, at least for GGCs, especially in the high-metallicity domain, we also considered

the scenario suggested by Carney (1996), showed in Figure 2b. In this panel only the measures listed by Carney (1996) have been plotted. In Section 9, we show which impact the use of the two proposed enhancement relations has on our results.

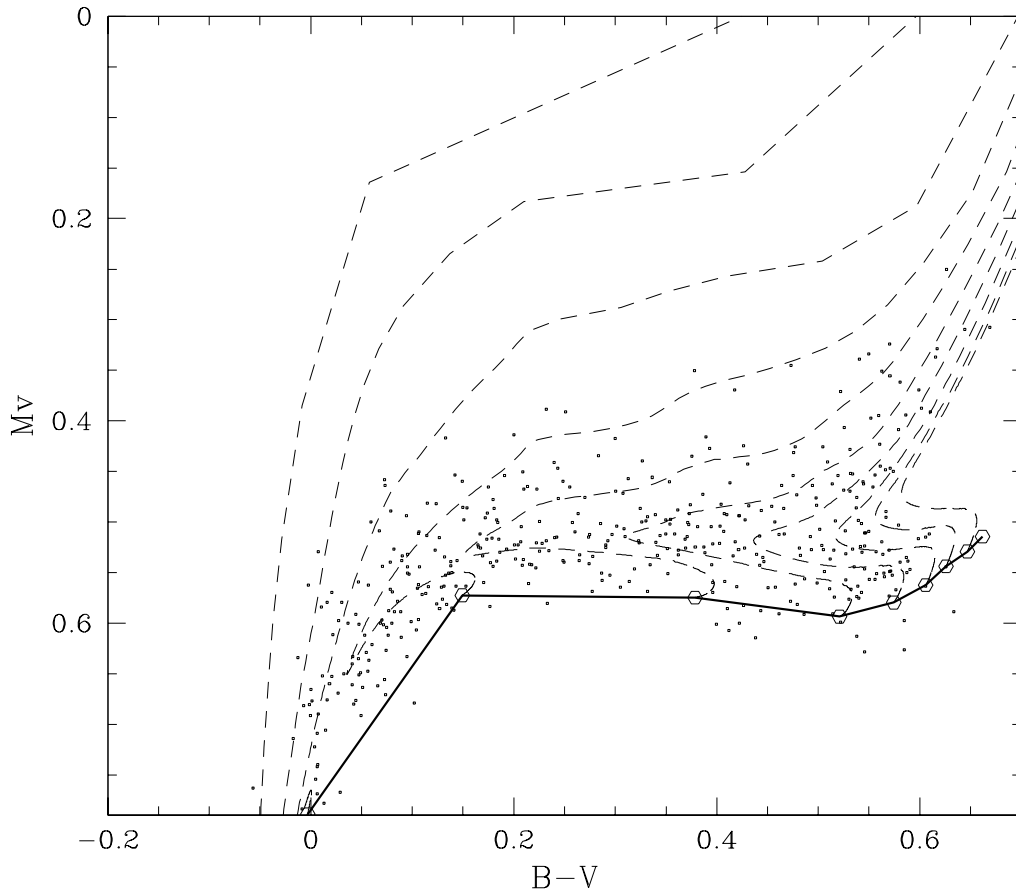


Fig. 4.— Evolutive tracks for $\text{Log}Z = -3.22$ are overplotted (as dashed lines) to a synthetic HB. The heavy solid line is the ZAHB.

On the theoretical side, Salaris, Chieffi & Straniero (1993) have investigated the effect produced on the theoretical evolutionary sequences by considering an enhancement of α -elements. They concluded that α -enhanced isochrones are well mimicked by the standard scaled-solar ones having global metallicity $[\text{M}/\text{H}]$ given by

$$[\text{M}/\text{H}] = [\text{Fe}/\text{H}] + \log(0.638f_{\alpha} + 0.362) \quad (1)$$

where f_α is the enhancement factor of the α -elements.

Taking into account these prescriptions we computed the global metallicity listed in column 4 of Table 1 as follows:

1. For the 19 GGCs with $[\alpha/\text{Fe}]$ listed by Salaris & Cassisi (1996) or Carney (1996) we adopted $f_\alpha = 10^{[\alpha/\text{Fe}]}$
2. For all the others, we assumed $f_\alpha = 10^{0.28}$ if $[\text{Fe}/\text{H}] < -0.8$ and $f_\alpha = 10^{-0.35[\text{Fe}/\text{H}]}$ if $[\text{Fe}/\text{H}] > -0.8$.

4. MODELING THE RGB AND THE HB: THE STATE OF THE ART

Understanding the observed properties of the HR-diagrams and luminosity functions of GCCs stars necessarily requires an homogeneous set of H and He-burning models of low mass stars and related isochrones. In this paper we have adopted the latest models computed by using the FRANEC (Frascati Raphson Newton Evolutionary Code) first described by Chieffi & Straniero (1989). The input physics has been recently updated (see e.g. Straniero, Chieffi & Limongi, 1997, SCL97). A subset of these models have been presented in SCL97, while the full set will be presented in a forthcoming paper (Chieffi, Limongi & Straniero 1998, hereafter CLS98).

The basic assumptions are here briefly summarized.

1. The radiative opacity coefficient is derived from the OPAL tables (Iglesias, Rogers & Wilson 1992) for temperatures larger than 10^4 K, and from Alexander & Ferguson (1994) at lower temperatures. Thermal conduction is taken from Itoh et al. (1983).
2. The equation of state (EOS) includes quantum-relativistic treatment of the electron plasma (electron degeneracy, pair production and the like). Coulomb corrections are evaluated by means of a Monte Carlo technique using a revised version of the Straniero (1988) EOS in which the partial degeneracy of the electron component is taken into account directly in the Monte Carlo calculations.
3. Thermal neutrinos rates due to plasma, photo and pair processes are taken into account following the prescription of Munakata, Kohyama & Itoh (1985), whereas Bremsstrahlung and recombination processes are included following Dicus et al (1976) and Beaudet, Petrosian & Salpeter (1967), respectively.
4. Nuclear reaction rates are derived from Caughlan & Fowler (1988), except for the $^{12}\text{C}(\alpha, \gamma)^{16}\text{O}$ for which the rate of Caughlan et al. (1985) is used.
5. The extension of the convective zones is determined by means of the classical Schwarzschild criterium. Induced overshooting and semiconvection during the central He-burning is also taken into account (see Castellani et al. 1985). The mixing length theory is adopted in order to evaluate the temperature gradient in the convective regions. The details of the mixing length calibrations can be found in SCL97. Breathing pulses occurring at the end of the central He burning phase have been inhibited by adopting the procedure described in Caputo et al (1989).

6. Microscopic diffusion of He and heavy elements have been included. Note that such a phenomenon mainly affects main sequence stars, while the properties of post MS evolution are only slightly changed (see SCL97 for more details).

Thus, models for masses ranging between 0.5 and $1.2 M_{\odot}$ have been computed from the ZAMS up to the the onset of the He-flash. The range of metallicity covers the typical value of the GGCs, namely $0.0001 \leq Z \leq 0.006$. A constant He, $Y = 0.23$, was adopted. Using these models we derived isochrones and luminosity functions for ages ranging between 8 and 20 Gyr.

For the HB, the present set includes models for masses ranging between 0.54 and $0.86 M_{\odot}$. The same chemical compositions of the corresponding H-burning models have been adopted. Following the usual procedure, the core masses and the surface compositions of the ZAHB models are derived from the corresponding last models of the H-burning sequences. Their evolution has been followed from the ZAHB up to the central He exhaustion. Few evolutionary sequences have been extended up to the first thermal pulse on the AGB. The procedure adopted to built the ZAHB is fully described by Castellani & Tornambe (1977). Breafly, the first model in our HB sequence have a fully homogeneous H-rich envelope, but the ZAHB model is set when all the secondary elements in the H-burning shell are relaxed to their equilibrium values. This happens when the zero age model has an age of $\sim 10^6$ yr. Then, the age of all the subsequent models have been rescaled to this zero point.

Finally, all the models have been transposed into the V , $(B - V)$ plane by means of the bolometric corrections and colour-temperature relations obtained by Bessel, Castelli & Pletz (1998a,b).

5. THE OBSERVED ZAHB LEVEL: A NEW METHODOLOGICAL APPROACH

Since the first wide series of HB models (Rood 1973), it is well known that the observed HB cannot be described by any single evolutionary track. It can rather be modelled by convolving a proper set of evolutionary paths of stars having slightly different values of total and/or core masses (Rood 1973). In other words, one can imagine the so-called Zero Age HB (ZAHB) as a sort of *starting locus* where stars are located after the helium ignition in the core, depending on their total and core mass, and from which they start their evolutionary run toward the AGB. It is thus quite simple (at least in principle) to accurately determine the location of the theoretical ZAHB.

On the observational side, measuring the ZAHB level is unfortunately fairly difficult and sometimes ambiguous. To minimize any possible evolutionary effects off the ZAHB, one might ideally define the ZAHB level by adopting the magnitude of the lower envelope of the observed HB distribution in the region with $0.2 < (B - V) < 0.6$.

However, the ‘‘HB levels’’ found in the literature are most often not compatible each other (and not directly comparable) as they actually are the mean level of the HB ($\langle V_{\text{HB}} \rangle$), or the mean magnitude of the RR Lyrae stars ($\langle V_{\text{RR}} \rangle$), or, finally, the ‘‘estimated’’ ZAHB level. Indeed, the frequent (implicit) assumption that $\langle V_{\text{RR}} \rangle$ is coincident with the ZAHB level has been largely criticized (see for example Lee, Demarque & Zinn, 1990) as the actual difference between these two quantities strongly depends on the HB morphology and, in turn, on metallicity (see Carney, Storm & Jones, 1992 and Cassisi & Salaris 1997).

Table 2. V_{ZAHB} , metallicities, reddening and derived DMs for the program GGCs.

<i>Name</i>	[Fe/H] _{Z85}	[Fe/H] _{CG97}	[M/H]	$E(B - V)$	V_{ZAHB}	$(M - m)_0^{CG97}$	$(M - m)_0^{[M/H]}$
NGC 104	-0.71	-0.70	-0.59	0.04	14.22±0.07	13.32	13.29
NGC 288	-1.40	-1.07	-0.85	0.03	15.50±0.10	14.73	14.67
NGC 362	-1.28	-1.15	-0.99	0.05	15.50±0.07	14.68	14.64
NGC1261	-1.31	-1.09	-0.89	0.02	16.72±0.05	15.98	15.93
NGC1466	-1.85	-1.64	-1.44	0.09	19.30±0.07	18.47	18.43
NGC1841	-2.20	-2.11	-1.91	0.18	19.42±0.10	18.39	18.36
NGC1851	-1.29	-1.08	-0.88	0.02	16.20±0.05	15.46	15.41
NGC1904	-1.69	-1.37	-1.22	0.01	16.27±0.07	15.63	15.60
NGC2419	-2.10	-1.97	-1.77	0.03	20.50±0.10	19.92	19.88
NGC2808	-1.37	-1.15	-0.95	0.23	16.27±0.07	14.90	14.85
NGC3201	-1.61	-1.23	-1.03	0.21	14.77±0.07	13.48	13.43
NGC4147	-1.80	-1.58	-1.38	0.02	16.95±0.10	16.32	16.28
NGC4372	-2.08	-1.94	-1.74	0.45	15.90±0.15	14.01	13.97
NGC4590	-2.09	-1.99	-1.81	0.04	15.75±0.05	15.14	15.11
NGC4833	-1.86	-1.58	-1.27	0.33	15.77±0.07	14.18	14.12
NGC5053	-2.58	-2.51	-2.31	0.03	16.70±0.07	16.19	16.17
NGC5272	-1.66	-1.34	-1.16	0.01	15.68±0.05	15.03	14.99
NGC5286	-1.79	-1.57	-1.37	0.24	16.60±0.10	15.29	15.25
NGC5466	-2.22	-2.14	-1.94	0.00	16.62±0.10	16.16	16.12
NGC5694	-1.91	-1.72	-1.52	0.09	18.70±0.10	17.88	17.84
NGC5824	-1.85	-1.64	-1.44	0.14	18.52±0.07	17.53	17.49
NGC5897	-1.68	-1.59	-1.44	0.08	16.45±0.07	15.64	15.61
NGC5904	-1.40	-1.11	-0.90	0.03	15.13±0.05	14.37	14.31
NGC5927	-0.31	-0.46	-0.37	0.47	16.72±0.10	14.41	14.39
NGC6093	-1.64	-1.41	-1.21	0.18	16.12±0.07	14.96	14.92
NGC6121	-1.33	-1.19	-0.94	0.36	13.45±0.10	11.68	11.62
NGC6171	-0.99	-0.87	-0.70	0.33	15.70±0.10	13.95	13.90
NGC6205	-1.65	-1.39	-1.18	0.02	15.10±0.15	14.43	14.38
NGC6218	-1.61	-1.37	-1.17	0.17	14.75±0.15	13.61	13.57
NGC6229	-1.54	-1.30	-1.10	0.01	18.11±0.05	17.45	17.41
NGC6254	-1.60	-1.41	-1.25	0.28	14.85±0.10	13.38	13.35
NGC6266	-1.28	-1.07	-0.87	0.47	16.40±0.20	14.26	14.21
NGC6333	-1.78	-1.56	-1.36	0.36	16.35±0.15	14.67	14.62
NGC6341	-2.24	-2.16	-1.95	0.02	15.30±0.10	14.78	14.74
NGC6352	-0.51	-0.64	-0.50	0.21	15.30±0.10	13.85	13.81
NGC6366	-0.99	-0.87	-0.70	0.69	15.80±0.10	12.93	12.88
NGC6397	-1.91	-1.82	-1.65	0.18	13.00±0.10	11.92	11.89
NGC6440	-0.34	-0.49	-0.40	1.09	18.70±0.20	14.48	14.45
NGC6528	-0.23	-0.38	-0.31	0.62	17.17±0.20	14.37	14.35
NGC6535	-1.75	-1.53	-1.33	0.32	15.90±0.15	14.33	14.29

Table 2—Continued

<i>Name</i>	[Fe/H] _{Z85}	[Fe/H] _{CG97}	[M/H]	$E(B - V)$	V_{ZAHB}	$(M - m)_0^{CG97}$	$(M - m)_0^{[M/H]}$
NGC6553	-0.29	-0.44	-0.36	0.84	16.92±0.20	13.46	13.44
NGC6584	-1.54	-1.30	-1.10	0.11	16.60±0.05	15.63	15.59
NGC6637	-0.59	-0.68	-0.55	0.17	15.95±0.10	14.64	14.60
NGC6652	-0.99	-0.87	-0.70	0.09	16.07±0.10	15.06	15.01
NGC6681	-1.51	-1.27	-1.07	0.07	15.85±0.10	15.00	14.95
NGC6712	-1.01	-0.88	-0.71	0.46	16.32±0.07	14.16	14.12
NGC6717	-1.32	-1.10	-0.90	0.21	15.75±0.15	14.43	14.38
NGC6752	-1.54	-1.42	-1.21	0.04	13.90±0.15	13.18	13.13
NGC6809	-1.82	-1.61	-1.41	0.07	14.60±0.10	13.82	13.78
NGC6838	-0.58	-0.70	-0.49	0.25	14.52±0.10	12.97	12.90
NGC6934	-1.54	-1.30	-1.10	0.11	16.97±0.07	16.00	15.96
NGC6981	-1.54	-1.30	-1.10	0.05	16.86±0.07	16.08	16.03
NGC7006	-1.59	-1.35	-1.15	0.05	18.85±0.15	18.08	18.03
NGC7078	-2.17	-2.12	-1.91	0.09	15.90±0.07	15.15	15.12
NGC7099	-2.13	-1.91	-1.71	0.03	15.30±0.10	14.71	14.67
NGC7492	-1.51	-1.27	-1.07	0.00	17.78±0.10	17.15	17.10
IC4499	-1.50	-1.26	-1.06	0.24	17.70±0.07	16.32	16.27
Rup 106	-1.90	-1.70	-1.50	0.21	17.85±0.10	16.66	16.62
Arp 2	-1.85	-1.64	-1.44	0.11	18.30±0.15	17.41	17.37
Ter 7	-0.49	-0.64	-0.52	0.06	17.87±0.10	16.89	16.85
Ter 8	-1.81	-1.60	-1.40	0.14	18.15±0.10	17.16	17.11

To overcome these ambiguities, we have developed a new procedure to re-determine the ZAHB level for all the GGCs listed in our catalog, so as to yield values which could be homogeneous and directly comparable with the corresponding theoretical ones. Using the full set of HB evolutionary tracks described in the previous section we generated a wide sample of synthetic HBs. The method and the code adopted to derive the synthetic HR-diagrams are described in a forthcoming paper (Chieffi, Straniero & Limongi 1998, in preparation). Briefly, to model an observed HB of a cluster with a given chemical composition this code requires several input parameters:

V_{lim} — the photometric limiting magnitude of the synthetic CMD

N_{HB} — the total number of stars with $V < V_{lim}$

M_{HB} — the mean mass of the HB stars (which drives the position in colour of the bulk of the star distribution along the ZAHB)

σ_M — the width of the gaussian mass distribution (which drives the spread in colour of the HB stars).

photometric errors— When comparing the synthetic HR-diagrams with the real ones, we have also to specify the photometric error bar the completeness of the stellar sample at different luminosity.

By properly tuning these quantities it is possible, in principle, to reproduce any observed HB morphology. For example, σ_M is the main parameter driving the presence and the extension of the HB blue tail. For example, in Figure 3 we show a set of synthetic HBs for 6 prototype clusters with different metallicity and, in turn, different HB morphologies. The horizontal line indicates the level of the ZAHB at $\log T_{\text{eff}} = 3.85$. As already noted, the lower envelope of the star distribution is not always coincident with the ZAHB level at $\log T_{\text{eff}} = 3.85$, and this confirms the need of a careful procedure to yield meaningful and comparable values for the ZAHB.

The problem is illustrated in a more appropriate scale in Figure 4 which shows the evolution of the HB stars off the ZAHB level. From inspecting this figure it is evident that the ZAHB level is not coincident with the lower envelope of the HB star distribution even when the HB is uniformly populated in the RR Lyrae region. This effect is mainly due to the fact that the evolution away from the ZAHB is quite rapid at the beginning. After only 8 Myr ($\sim 8\%$ of the total lifetime in HB) the stars are already 0.05–0.1 mag brighter than the ZAHB *starting line*, then they spend $\sim 70\%$ of the total HB time in covering the next 0.1 mag. Thus the near-ZAHB HB is inherently poorly populated and the observed lower envelope of the HB will be a poor measure of the “HB level” which is affected both by the sample size and the size of the photometric errors.

To overcome the problem we have adopted the following empirical procedure:

1. For each cluster in our catalog we computed a synthetic HB (with the appropriate abundances) tuning the parameters so as to best reproduce the observed HB morphology.
2. The synthetic HB has been shifted in magnitude and colour to match the observed HB.
3. The “observed” V_{ZAHB} value is then read from the line indicating the theoretical ZAHB level at $\log T_{\text{eff}} = 3.85$ as yielded by the best-fitting synthetic HB.

Note that this procedure does makes use of the models only as a guide to drawing of the location of the “true” ZAHB level and is only slightly dependent on the adopted theoretical models. It avoids the uncertainties induced by the differences in the observed HB morphologies and yields values obtained with a homogeneous and self-consistent empirical method. ZAHB levels determined in this way should be especially appropriate to compare with theoretical models. The V_{ZAHB} value thus obtained are listed in column 6 of Table 2. The errors in V_{ZAHB} has been estimated by combining the scatter from multiple independent determinations of the ZAHB level and an estimate of the photometric error (at the HB level) in each individual cluster.

Although the actual difference between V_{ZAHB} and $\langle V_{\text{HB}} \rangle$ depends on the various parameters (like the mean star mass, the core mass, the metallicity, helium abundance, etc) which drive the HB morphology, on the base of the synthetic HB plotted in Figure 3 and Figure 4 we derived the following average relation:

$$V_{\text{ZAHB}} = \langle V_{\text{HB}} \rangle + 0.106[\text{M}/\text{H}]^2 + 0.236[\text{M}/\text{H}] + 0.193 \quad (2)$$

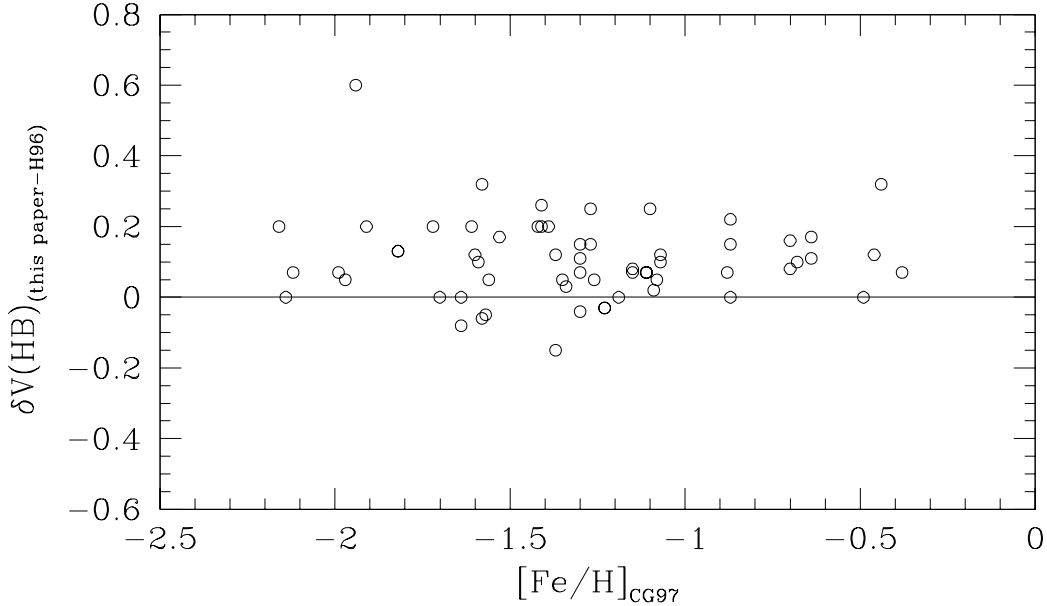


Fig. 5.— Differences between the V_{ZAHB} level obtained in this paper and the $V(HB)$ listed by H96.

which can be used, at a first order, to derive the V_{ZAHB} level from the $\langle V_{HB} \rangle$ measured in the colour range $0.2 < (B - V) < 0.6$. Note that for metal rich clusters ($[M/H] > -1$) the mean value of the red HB clump was assumed as $\langle V_{HB} \rangle$. The relation suggests that the minimum difference between ZAHB and mean HB luminosity ($\delta V \sim 0.06$) occurs at $[M/H] \sim -1.2$, and it turns to be $\delta V \sim 0.16$ and ~ 0.10 at $[M/H] = -2.2$ and -0.5 , respectively.

We can compare the adopted V_{ZAHB} values listed in Table 2, for instance, with those listed in the recent compilation by Harris (1996) (hereafter H96). The residuals (this paper – H96) are plotted versus $[Fe/H]_{CG97}$ in Figure 5. As expected, there is a clear systematic difference (~ 0.17 mag) between the two, with the values derived in this paper being fainter than those listed by H96. Only one cluster (NGC 4372) shows a large ($\delta V > 0.4$) residual. This is due to the fact that H96 adopted a different (older) photometry (with a different photometric zero-point) than that used in this paper. Similar comparisons can be made with other compilations (Buonanno, Corsi & Fusi

Pecci 1989, Chaboyer, Demarque & Sarajedini, 1996). In both cases V_{HB} values listed in Table 2 are systematically fainter ($\delta V \sim 0.1$ and $\delta V \sim 0.15$, respectively).

6. THE RED GIANT BRANCH

6.1. The RGB mean ridge line

In order to derive the mean ridge line of the RGB for all the GGCs listed in our catalog we adopted the following procedure:

1. A rough preliminary selection of the stars belonging to the RGB (excluding the HB and AGB stars) has been performed by eye to initialize and to accelerate the subsequent iterations.
2. The polynomial fitting technique presented by Sarajedini & Norris (1994, hereafter SN94) has then be applied to the samples. In particular, the RGB has been fitted by a (2nd or 3rd order) polynomial law in the form $(B - V) = f(V)$. After each iteration stars more than $2\text{-}\sigma$ in colour from the best-fitting ridge line were rejected and the fitting procedure repeated to yield a stable solution.

6.2. Photometric parameters along the RGB

As widely known, RGB morphology and location in the CMD are good metallicity indicators of the parent cluster. In particular three main parameters have been defined to describe the photometric characteristics of the RGB:

ΔV – First defined by Sandage and Wallerstein (1960), as a measure of the height of the RGB brighter than the HB level. They used $\Delta V_{1.4}$ (in mag.), with V_{RGB} measured at the intrinsic colour $(B - V)_0 = 1.4$. Recently, Sarajedini & Layden (1997, SL97) have defined two similar parameters, $\Delta V_{1.1}$ and $\Delta V_{1.2}$, measured at $(B - V)_0 = 1.1$ and $(B - V)_0 = 1.2$, respectively. These two additional parameters are particularly useful since the observed samples are often not populated enough at $(B - V)_0 = 1.4$ to clearly define a mean ridge line.

$(B - V)_{0,g}$ – Defined by Sandage and Smith (1966) as the intrinsic colour of the RGB at the HB level.

S – Defined by Hartwick (1968) (and here called $S_{2.5}$) as the slope of the line connecting two points along the RGB: the first being intersection of the RGB with the line defining the HB level and the second being the point on the RGB 2.5 mag brighter than the HB. Following SL97, we have also defined $S_{2.0}$ which is based on the the RGB point only 2.0 mag brighter than the HB level.

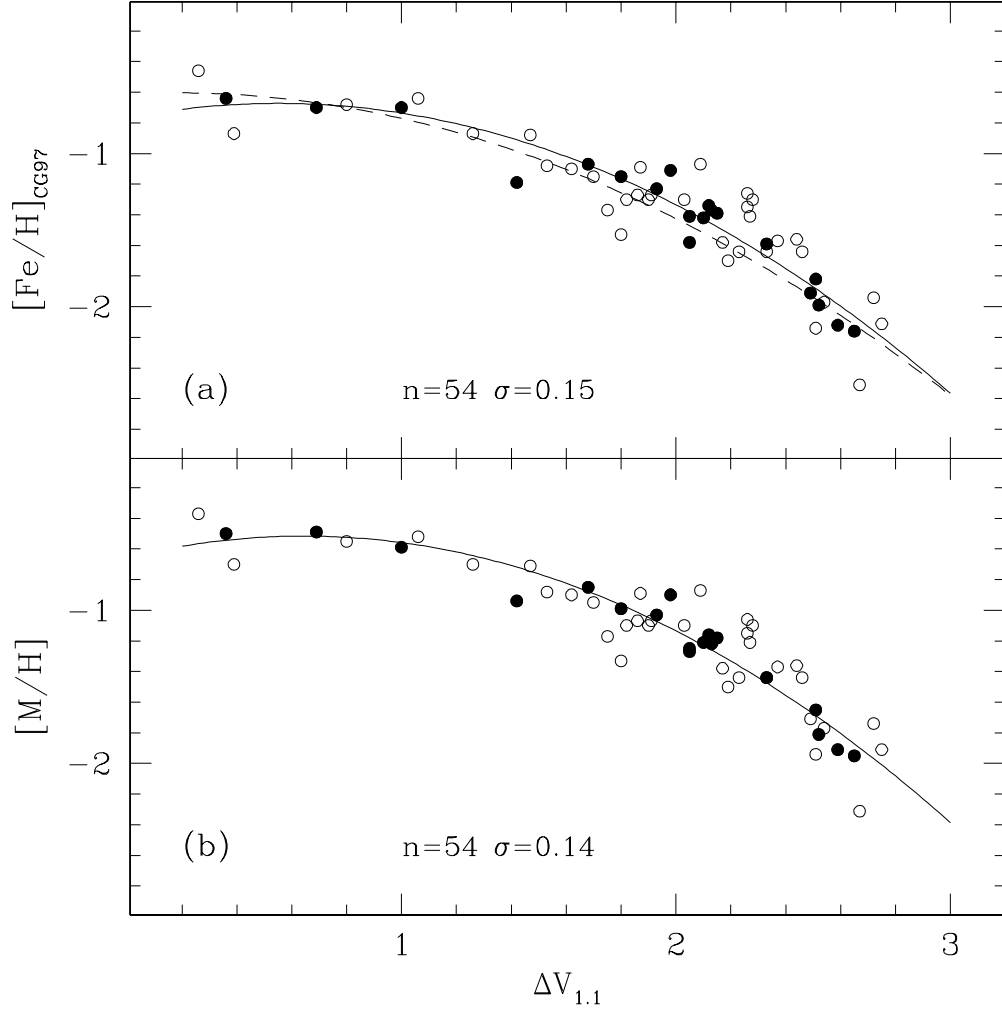


Fig. 6.— Calibration of the $\Delta V_{1.1}$ parameter with respect $[\text{Fe}/\text{H}]_{\text{CG97}}$ (*panel (a)*) and the global metallicity ($[\text{M}/\text{H}]$) (*panel (b)*). The filled symbols represent clusters for which spectroscopic metallicity and $[\alpha/\text{Fe}]$ abundance has been directly measured. The solid lines are the best fit to the data. The dashed line in *panel (a)* is the relation recently obtained by Carretta & Bragaglia 1998. The number of clusters used to compute each relation is reported together with the standard deviations of the data.

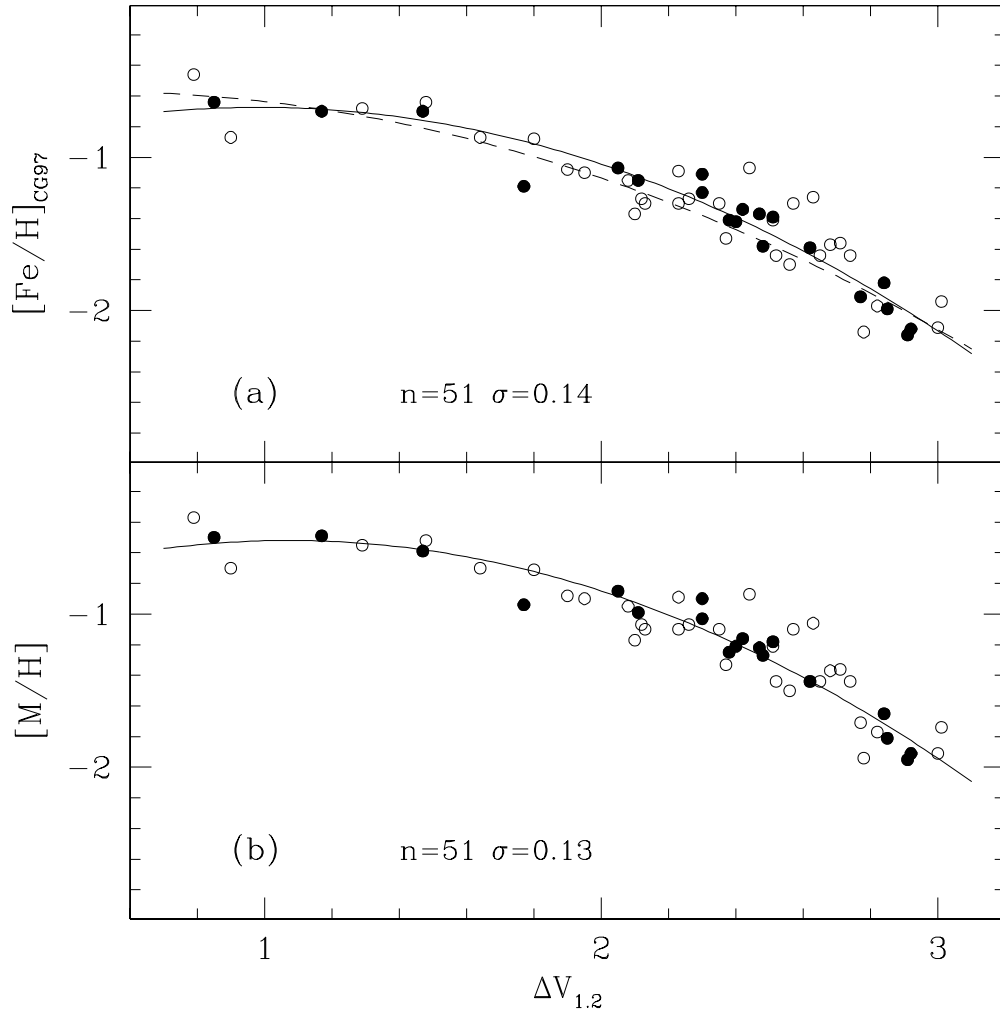


Fig. 7.— Calibration of the $\Delta V_{1,2}$ parameter with respect $[\text{Fe}/\text{H}]_{\text{CG97}}$ (*panel (a)*) and the global metallicity ($[\text{M}/\text{H}]$) (*panel (b)*). The symbols have the same meaning of Figure 6.

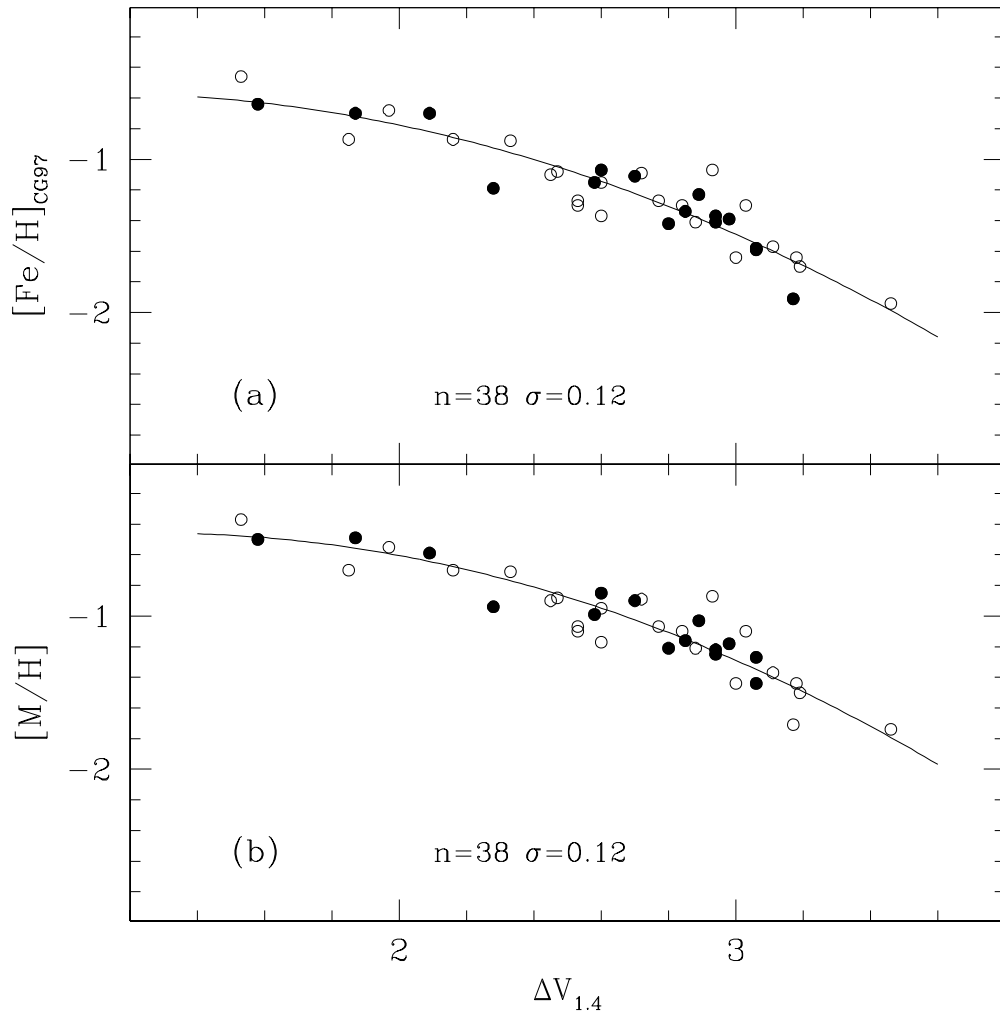


Fig. 8.— Calibration of the $\Delta V_{1.4}$ parameter with respect $[\text{Fe}/\text{H}]_{\text{CG97}}$ (*panel (a)*) and the global metallicity ($[\text{M}/\text{H}]$) (*panel (b)*). The symbols have the same meaning of Figure 6.

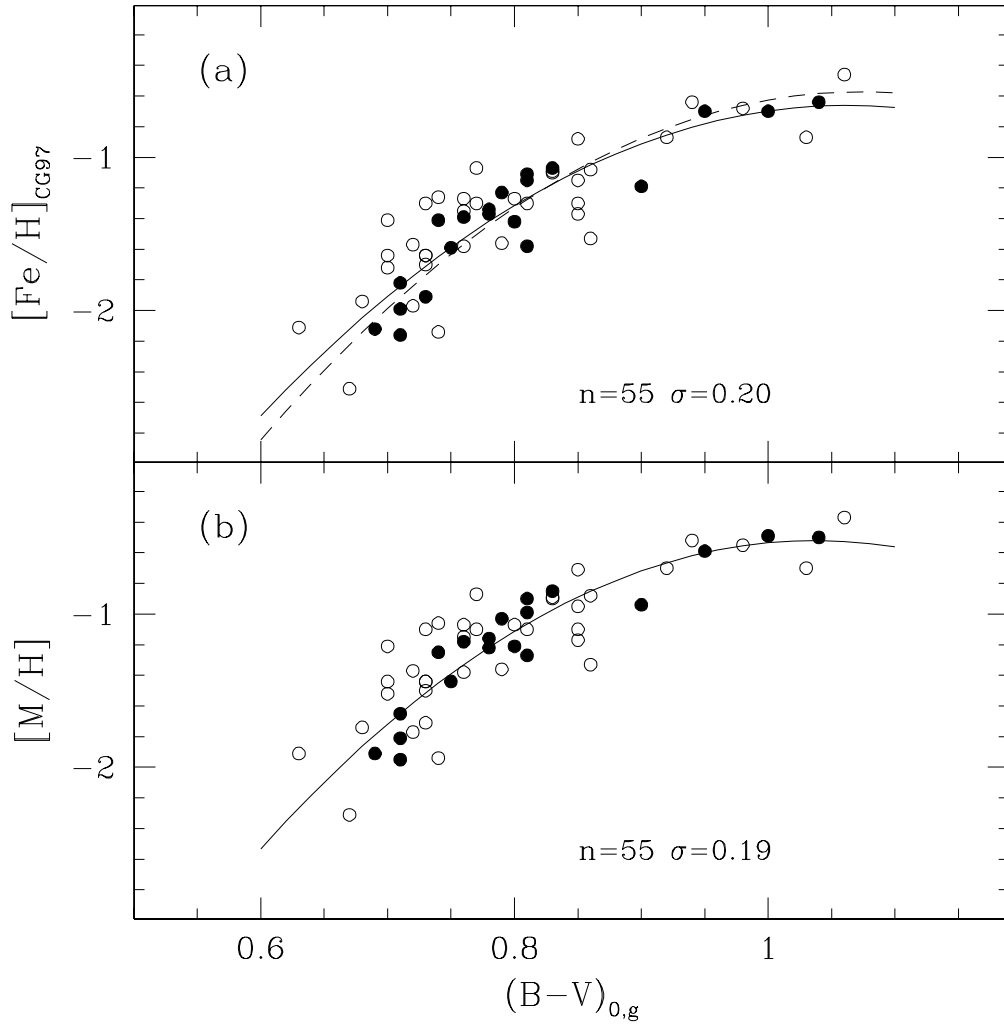


Fig. 9.— Calibration of the $(B-V)_{0,g}$ parameter with respect $[\text{Fe}/\text{H}]_{\text{CG97}}$ (*panel (a)*) and the global metallicity ($[\text{M}/\text{H}]$) (*panel (b)*). The symbols have the same meaning of Figure 6.

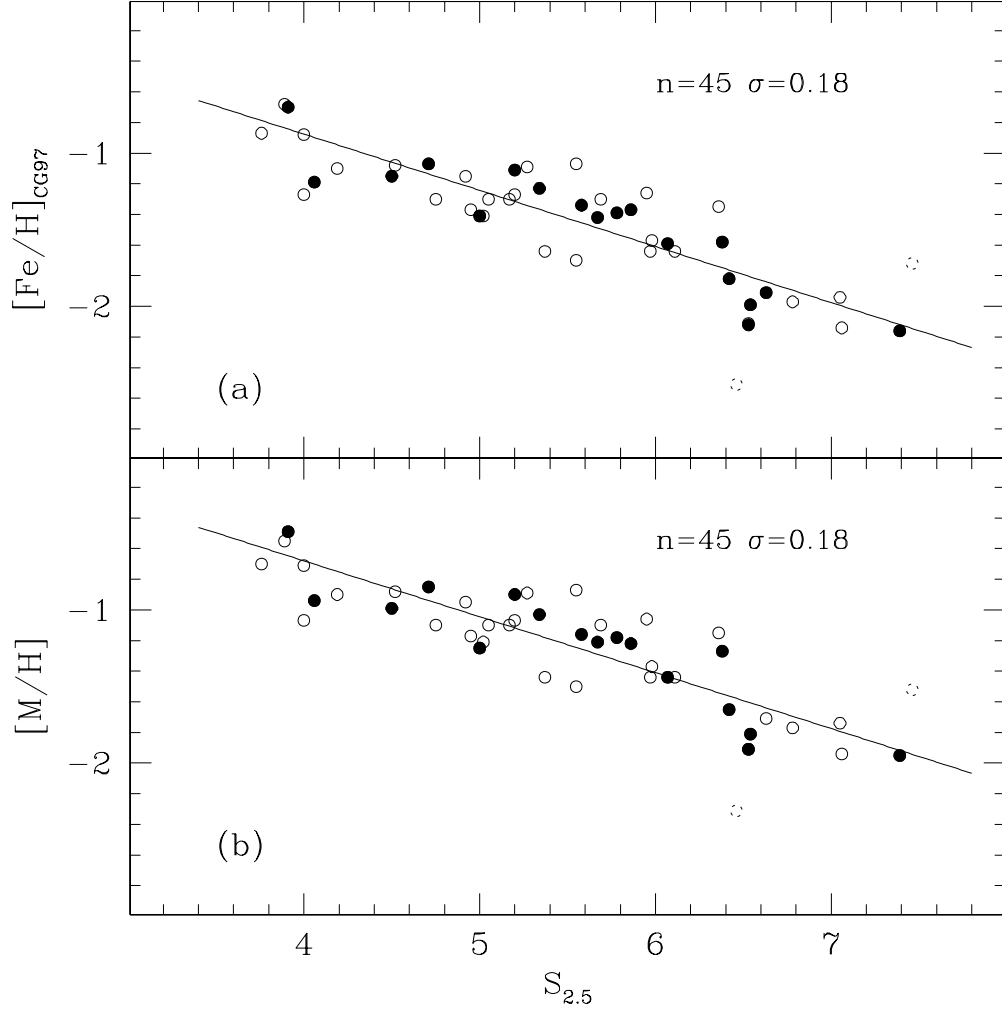


Fig. 10.— Calibration of the $S_{2.5}$ parameter with respect $[\text{Fe}/\text{H}]_{\text{CG97}}$ (*panel (a)*) and the global metallicity ($[\text{M}/\text{H}]$) (*panel (b)*). The symbols have the same meaning of Figure 6. Two clusters (namely NGC 5053 and NGC 5694, plotted as dotted circles), have been excluded in the determination of the fitting relation (see text).

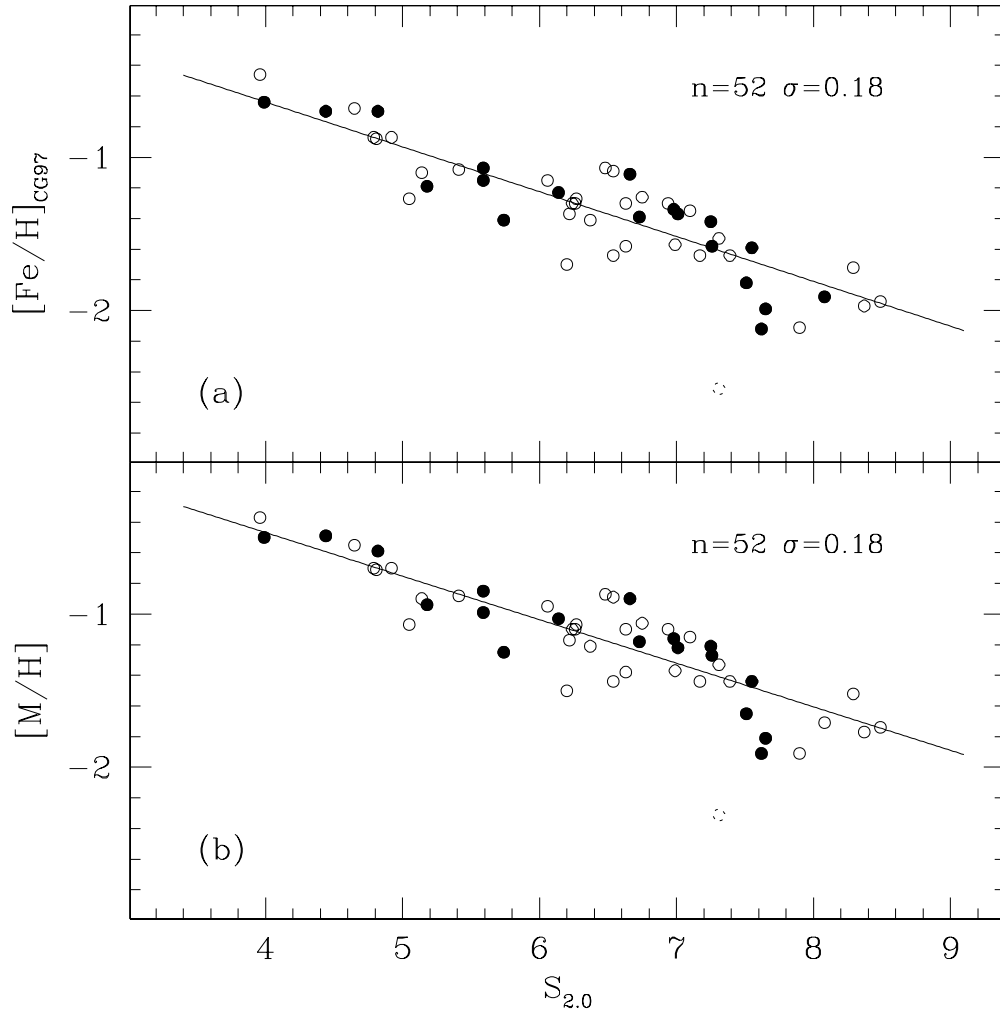


Fig. 11.— Calibration of the $S_{2.0}$ parameter with respect $[\text{Fe}/\text{H}]_{\text{CG97}}$ (*panel (a)*) and the global metallicity ($[\text{M}/\text{H}]$) (*panel (b)*). The symbols have the same meaning of Figure 6.

Table 3. RGB parameters.

<i>Name</i>	[Fe/H] _{CG97}	[M/H]	$\Delta V_{1.1}$	$\Delta V_{1.2}$	$\Delta V_{1.4}$	(B-V) _{0,g}	$S_{2.5}$	$S_{2.0}$	(B - V) _{0,-1}
NGC 104	-0.70	-0.59	1.00	1.47	2.09	0.95	—	4.82	1.29
NGC 288	-1.07	-0.85	1.68	2.05	2.60	0.83	4.71	5.59	1.12
NGC 362	-1.15	-0.99	1.80	2.11	2.58	0.81	4.50	5.59	1.07
NGC1261	-1.09	-0.89	1.87	2.23	2.72	0.83	5.27	6.54	1.07
NGC1466	-1.64	-1.44	2.23	2.52	3.00	0.73	5.37	6.54	0.93
NGC1841	-2.11	-1.91	2.75	3.00	—	0.63	6.53	7.90	0.80
NGC1851	-1.08	-0.88	1.53	1.90	2.47	0.86	4.52	5.41	1.15
NGC1904	-1.37	-1.22	2.13	2.47	2.94	0.78	5.86	7.01	1.00
NGC2419	-1.97	-1.77	2.54	2.82	—	0.72	6.78	8.37	0.88
NGC2808	-1.15	-0.95	1.70	2.08	2.60	0.85	4.92	6.06	1.10
NGC3201	-1.23	-1.03	1.93	2.30	2.89	0.79	5.34	6.14	1.05
NGC4147	-1.58	-1.38	2.17	—	—	0.76	—	6.63	0.99
NGC4372	-1.94	-1.74	2.72	3.01	3.46	0.68	7.05	8.49	0.83
NGC4590	-1.99	-1.81	2.52	2.85	—	0.71	6.54	7.65	0.88
NGC4833	-1.58	-1.27	2.05	2.48	3.06	0.81	6.38	7.26	1.01
NGC5053	-2.51	-2.31	2.67	—	—	0.67	6.46	7.31	0.84
NGC5272	-1.34	-1.16	2.12	2.42	2.85	0.78	5.58	6.98	0.99
NGC5286	-1.57	-1.37	2.37	2.68	3.11	0.72	5.98	6.99	0.93
NGC5466	-2.14	-1.94	2.51	2.78	—	0.74	7.06	9.44	0.86
NGC5694	-1.72	-1.52	—	—	—	0.70	7.46	8.29	0.87
NGC5824	-1.64	-1.44	2.46	2.74	3.18	0.70	6.11	7.39	0.89
NGC5897	-1.59	-1.44	2.33	2.62	3.06	0.75	6.07	7.55	0.93
NGC5904	-1.11	-0.90	1.98	2.30	2.70	0.81	5.20	6.66	1.04
NGC5927	-0.46	-0.37	0.26	0.79	1.53	1.06	—	3.96	1.52
NGC6093	-1.41	-1.21	2.27	2.51	2.88	0.70	5.02	6.37	0.92
NGC6121	-1.19	-0.94	1.42	1.77	2.28	0.90	4.06	5.18	1.18
NGC6171	-0.87	-0.70	1.26	1.64	2.16	0.92	3.76	4.92	1.24
NGC6205	-1.39	-1.18	2.15	2.51	2.98	0.76	5.78	6.73	0.98
NGC6218	-1.37	-1.17	1.75	2.10	2.60	0.85	4.95	6.22	1.08
NGC6229	-1.30	-1.10	1.82	2.13	2.53	0.85	4.75	6.63	1.07
NGC6254	-1.41	-1.25	2.05	2.38	2.94	0.74	5.00	5.74	1.00
NGC6266	-1.07	-0.87	2.09	2.44	2.93	0.77	5.55	6.48	1.02
NGC6333	-1.56	-1.36	2.44	2.71	—	0.79	—	—	0.92
NGC6341	-2.16	-1.95	2.65	2.91	—	0.71	7.39	9.74	0.83
NGC6352	-0.64	-0.50	0.36	0.85	1.58	1.04	—	3.99	1.49
NGC6366	-0.87	-0.70	0.39	0.90	1.85	1.03	—	4.79	1.38
NGC6397	-1.82	-1.65	2.51	2.84	—	0.71	6.42	7.51	0.89
NGC6440	-0.49	-0.40	—	—	—	—	—	—	—
NGC6528	-0.38	-0.31	—	—	—	—	—	—	—
NGC6535	-1.53	-1.33	1.80	2.37	—	0.86	—	7.31	1.07

Table 3—Continued

<i>Name</i>	[Fe/H] _{CG97}	[M/H]	$\Delta V_{1.1}$	$\Delta V_{1.2}$	$\Delta V_{1.4}$	$(B-V)_{0,g}$	$S_{2.5}$	$S_{2.0}$	$(B-V)_{0,-1}$
NGC6553	-0.44	-0.36	—	—	—	—	—	—	—
NGC6584	-1.30	-1.10	2.03	2.35	2.84	0.77	5.17	6.24	1.01
NGC6637	-0.68	-0.55	0.80	1.29	1.97	0.98	3.89	4.65	1.35
NGC6652	-0.87	-0.70	—	—	—	—	—	—	—
NGC6681	-1.27	-1.07	1.91	2.26	2.77	0.80	5.20	6.27	1.05
NGC6712	-0.88	-0.71	1.47	1.80	2.33	0.85	4.00	4.81	1.19
NGC6717	-1.10	-0.90	1.62	1.95	2.45	0.83	4.19	5.14	1.13
NGC6752	-1.42	-1.21	2.10	2.40	2.80	0.80	5.67	7.25	1.00
NGC6809	-1.61	-1.41	—	—	—	—	—	—	—
NGC6838	-0.70	-0.49	0.69	1.17	1.87	1.00	3.91	4.44	1.39
NGC6934	-1.30	-1.10	2.28	2.57	3.03	0.73	5.69	6.94	0.95
NGC6981	-1.30	-1.10	1.90	2.23	—	0.81	5.05	6.26	1.04
NGC7006	-1.35	-1.15	2.26	—	—	0.76	6.36	7.10	0.98
NGC7078	-2.12	-1.91	2.59	2.92	—	0.69	6.53	7.62	0.86
NGC7099	-1.91	-1.71	2.49	2.77	3.17	0.73	6.63	8.08	0.89
NGC7492	-1.27	-1.07	1.86	2.12	2.53	0.76	4.00	5.05	1.04
IC4499	-1.26	-1.06	2.26	2.63	—	0.74	5.95	6.75	0.97
Rup 106	-1.70	-1.50	2.19	2.56	3.19	0.73	5.55	6.20	0.96
Arp 2	-1.64	-1.44	2.33	2.65	—	0.73	5.97	7.17	0.92
Ter 7	-0.64	-0.52	1.06	1.48	—	0.94	—	—	1.30
Ter 8	-1.60	-1.40	—	—	—	—	—	—	—

Over the past 15 years many calibrations of these parameters in terms of metallicity have been proposed (see Table 5 in Ferraro, Fusi Pecci & Buonanno 1992 and, recently, SL97, Carretta & Bragaglia 1998, and Table 7 by Borissova et al 1999). We present here revised calibrations making use of the wider and more homogeneous data-set now available. The six parameters defined above (namely, $\Delta V_{1.1}$, $\Delta V_{1.2}$, $\Delta V_{1.4}$, $(B-V)_{0,g}$, $S_{2.0}$, $S_{2.5}$) have been measured for all the GGCs listed in our catalog and having suitable data in the $(V, B-V)$ plane. No attempt has been performed to extrapolate the mean ridge line beyond the sufficiently populated regions of the available CMDs. The values measured are listed in Table 3. The main source of uncertainty in these measures is the propagation of the the error in the determination of the ZAHB level. Thus, the uncertainty on the V_{ZAHB} (~ 0.10) typically produces a comparable uncertainty ($\delta \sim 0.1$ mag) in measuring ΔV -parameters, an error $\delta \sim 0.03$ mag in the determination of the colour $(B-V)_{0,g}$, and a significantly larger error ($\delta \sim 0.2 - 0.3$) in deriving the S parameters.

In Figure 6–11 a,b, the RGB-observables are plotted versus the metal abundances $[\text{Fe}/\text{H}]_{\text{CG97}}$ (panel (a)) and the global metallicities $[\text{M}/\text{H}]$ (panel (b)). The solid line overplotted in each Figure the best fits to the data given in analytic form in Table 4. In deriving these relations, the 20 GGCs with direct spectroscopic measures of $[\text{Fe}/\text{H}]$ and direct measures of the $[\alpha/\text{Fe}]$ abundance

(excepting NGC 7099) have been considered as *primary calibrators* and have been assumed with higher weights in determining the best fit relations. These primary calibrators are plotted as filled circles. Two clusters (NGC 5053 and NGC 5694) which have the largest deviations in Figure 10 (plotted as dotted circles) have been excluded during the fitting procedure. In both of the excluded clusters the observed samples the upper RGB is so poorly populated that the location of the branch at that level is quite uncertain. NGC 5053 has been excluded, for the same reason, in deriving the calibration of the parameter $S_{2,0}$ (see Figure 11). The relationships of all the RGB parameters defined above in terms of the spectroscopic and *global* metallicity scales are reported in Table 4. Note that the quoted relations can be safely used only in the metallicity range covered by the adopted sample (i.e. roughly $-2.5 < [\text{Fe}/\text{H}]_{\text{CG97}} < -0.5$ and $-2.3 < [\text{M}/\text{H}] < -0.4$). This range should be considered as a first guess and the reader is requested to refer to each figure (Figure 6–11) to check the exact range of metallicity within which each relation has been derived.

Table 4. RGB parameters and their calibration in terms of different metallicity scales.

Relations in terms of $[\text{Fe}/\text{H}]_{\text{CG97}}$		
$[\text{Fe}/\text{H}]_{\text{CG97}} = -0.315\Delta V_{1,1}^2 + 0.347\Delta V_{1,1} - 0.768$	n=54 $\sigma = 0.15$	(4.1)
$[\text{Fe}/\text{H}]_{\text{CG97}} = -0.359\Delta V_{1,2}^2 + 0.708\Delta V_{1,2} - 1.023$	n=51 $\sigma = 0.14$	(4.2)
$[\text{Fe}/\text{H}]_{\text{CG97}} = -0.252\Delta V_{1,4}^2 + 0.548\Delta V_{1,4} - 0.864$	n=38 $\sigma = 0.12$	(4.3)
$[\text{Fe}/\text{H}]_{\text{CG97}} = -9.47(B - V)_{0,g}^2 + 20.127(B - V)_{0,g} - 11.36$	n=55 $\sigma = 0.20$	(4.4)
$[\text{Fe}/\text{H}]_{\text{CG97}} = -0.37S_{2,5} + 0.59$	n=45 $\sigma = 0.18$	(4.5)
$[\text{Fe}/\text{H}]_{\text{CG97}} = -0.28S_{2,0} + 0.67$	n=52 $\sigma = 0.18$	(4.6)
$(B - V)_{0,g} = 0.005[\text{Fe}/\text{H}]_{\text{CG97}}^3 + 0.118[\text{Fe}/\text{H}]_{\text{CG97}}^2 + 0.489[\text{Fe}/\text{H}]_{\text{CG97}} + 1.243$	n=55 $\sigma = 0.04$	(4.7)
Relations in terms of $[\text{M}/\text{H}]$		
$[\text{M}/\text{H}] = -0.337\Delta V_{1,1}^2 + 0.434\Delta V_{1,1} - 0.656$	n=54 $\sigma = 0.14$	(4.8)
$[\text{M}/\text{H}] = -0.382\Delta V_{1,2}^2 + 0.820\Delta V_{1,2} - 0.960$	n=51 $\sigma = 0.13$	(4.9)
$[\text{M}/\text{H}] = -0.280\Delta V_{1,4}^2 + 0.717\Delta V_{1,4} - 0.918$	n=38 $\sigma = 0.12$	(4.10)
$[\text{M}/\text{H}] = -10.513(B - V)_{0,g}^2 + 21.813(B - V)_{0,g} - 11.835$	n=55 $\sigma = 0.19$	(4.11)
$[\text{M}/\text{H}] = -0.36S_{2,5} + 0.78$	n=45 $\sigma = 0.18$	(4.12)
$[\text{M}/\text{H}] = -0.29S_{2,0} + 0.53$	n=52 $\sigma = 0.18$	(4.13)
$(B - V)_{0,g} = 0.04[\text{M}/\text{H}]^3 + 0.275[\text{M}/\text{H}]^2 + 0.67[\text{M}/\text{H}] + 1.252$	n=55 $\sigma = 0.04$	(4.14)
The parameter $(B - V)_{0,-1}$ vs metallicity		
$(B - V)_{0,-1} = 0.055[\text{Fe}/\text{H}]_{\text{CG97}}^3 + 0.448[\text{Fe}/\text{H}]_{\text{CG97}}^2 + 1.255[\text{Fe}/\text{H}]_{\text{CG97}} + 2.023$	n=55 $\sigma = 0.05$	(4.15)
$(B - V)_{0,-1} = 0.115[\text{M}/\text{H}]^3 + 0.695[\text{M}/\text{H}]^2 + 1.496[\text{M}/\text{H}] + 1.983$	n=55 $\sigma = 0.05$	(4.16)

Similar relations for $\Delta V_{1.1}$, $\Delta V_{1.2}$ and $(B - V)_{0,g}$ have been recently obtained by Carretta & Bragaglia (1998), who used the values listed by SL97 and SN94. For sake of comparison, their relations have been plotted as dashed lines in the corresponding Figures. The differences can easily be understood as due to the combination of two main factors:

1. The different assumptions on the HB level; there are differences up to 0.15 mag between the HB levels adopted here and those listed in SL97 and SN94. These differences directly affect the measure of ΔV parameters, and this explains most of the offset between the solid and the dashed lines in Figure 5a,6a.
2. The small sample (only 9 GGCs) considered by Carretta & Bragaglia (1998); this mainly affects the fit at the extremes. In fact, the dashed lines significantly deviate from the solid line at the extremes of the metallicity scale (see Figure 6a,7a,9a).

6.3. The SRM in the $(V, B - V)$ plane

The equations reported in Table 4 represent a system which can be used to *simultaneously* derive very useful estimates of metal abundance ($[\text{Fe}/\text{H}]_{\text{CG97}}$ and $[\text{M}/\text{H}]$) and reddening from the morphology and location of the RGB (the so-called SRM Method, Sarajedini 1994b). By using the system of equations in Table 4 one can choose the most appropriate observables (measurable in the CMD depending on the actual extension of the observed RGB) and then proceed as follows:

1. Since parameters $S_{2.0}$ and $S_{2.5}$ are independent of cluster reddening, from eq.s 4.5 and 4.6 it is possible to obtain a first guess of the cluster metallicity $[\text{Fe}/\text{H}]_i$, and similarly $[\text{M}/\text{H}]_i$ using eq.s 4.12 and 4.13.
2. Introducing then $[\text{Fe}/\text{H}]_i$ in eq. 4.7 it is possible to derive a first value for the expected $(B - V)_{0,g}$ and, in turn, a first estimate for the reddening from $E(B - V) = (B - V)_g - (B - V)_{0,g}$.
3. Using this first estimate of the reddening it is then possible to derive $\Delta V_{1.1}$, $\Delta V_{1.2}$, $\Delta V_{1.4}$, and from eq.s 4.1, 4.2 and 4.3 a new determination of the metallicity.
4. By iterating the procedure one can quickly achieve convergence, yielding values for reddening and the metallicities generally accurate at about $\delta[\text{Fe}/\text{H}] < 0.1$ and $\delta E(B - V) < 0.02$.

6.4. The RGB-bump: the new data-base

One of the most intriguing features along the RGB is the so-called RGB-bump whose existence was predicted since the early theoretical models (Thomas 1967, Iben 1968) but was first observed years later (King, Da Costa & Demarque, 1985) the observed samples were not populous enough to allow a firm detection. In fact a very large sample of stars, with more than 1000 in the upper 4 mag. of the RGB, is necessary to safely distinguish this feature from statistical fluctuations. This problem is more severe for metal poor clusters, due to the dependance of the luminosity of the bump on metallicity: the luminosity increases with decreasing metallicity. So, in metal poor GGCs

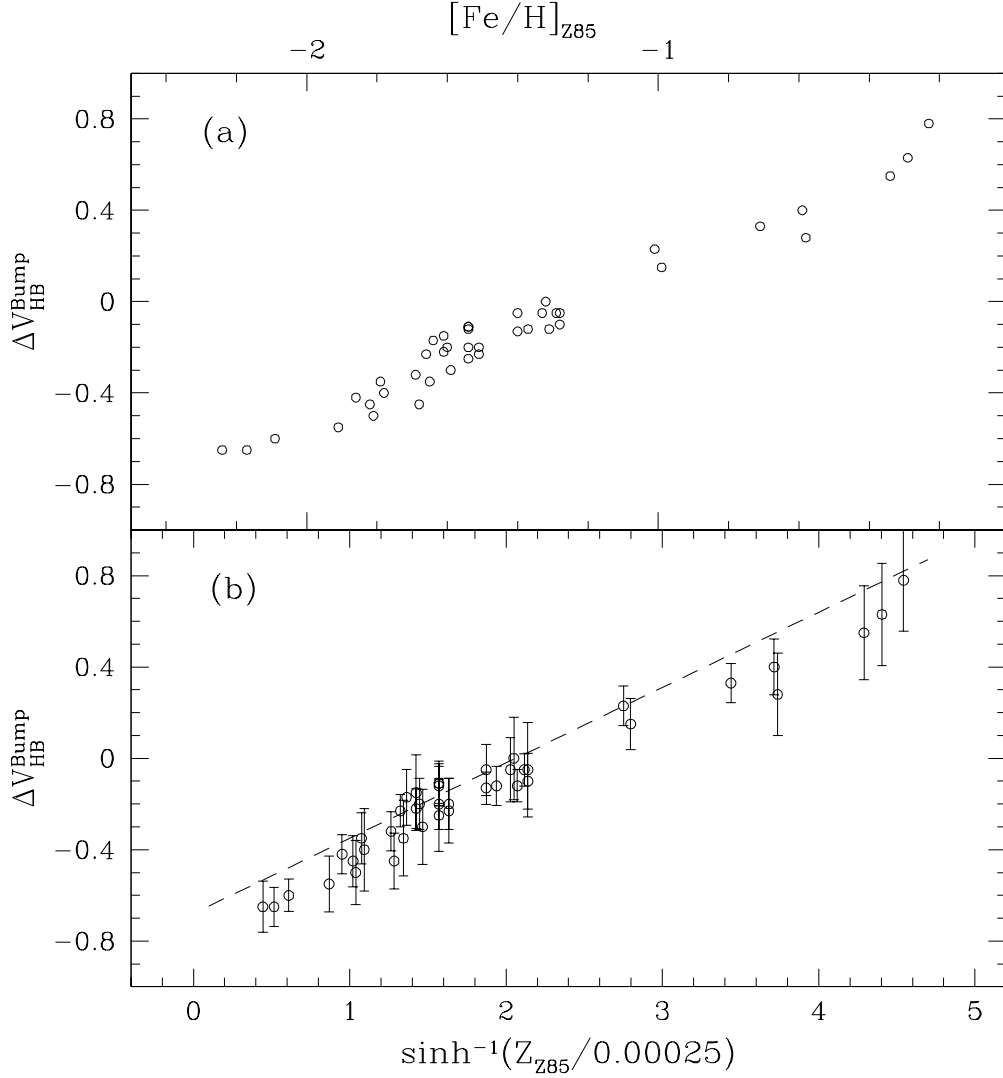


Fig. 12.— The ΔV_{HB}^{Bump} parameter as function of the metallicity ($[Fe/H]_{Z85}$) and the parameter s (panel (a) and (b), respectively). The dashed line is the relation obtained by F90.

the bump is shifted toward the RGB tip, in a region which is intrinsically poorly populated, and where the detection is difficult even when large samples are available.

The first systematic study of the location of the RGB-Bump in GGCs has been presented by Fusi Pecci et al. (1990, hereafter F90), who reported the identification of the bump in a sample of 11 GGCs. They presented a detailed comparison with theoretical models (Rood & Crocker

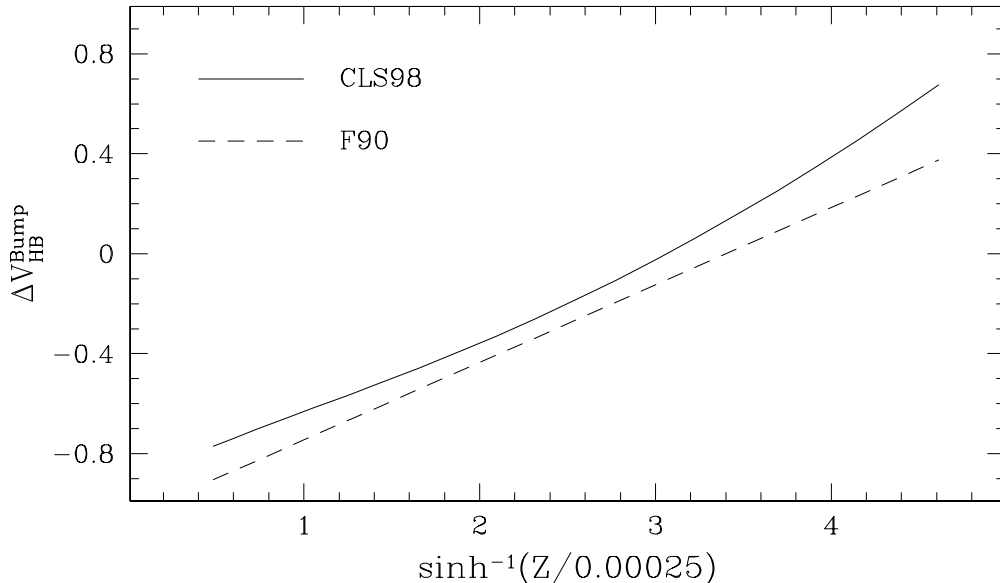


Fig. 13.— *New* and *old* theoretical $\Delta V_{\text{HB}}^{\text{Bump}}$ as function of s : present models SLC98 (solid line) and the relation adopted by F90 (dashed line).

1989, Rood unpublished) based on old input physics. This first comparison showed that while the dependence of bump luminosity on metallicity was nicely reproduced by theoretical models, there was a substantial disagreement in the zero-point, the theoretical relation being about 0.4 mag brighter than the observations. Alongi et al. (1991) interpreted this disagreement as an evidence of the limit of the standard models in describing the correct location of the RGB-bump. Thus, in order to reconcile observations and theory, they claimed the occurrence of an additional mixing process below the bottom of the convective envelope of an RGB star (i.e. *under-shooting*). However, Straniero, Chieffi & Salaris (1992) and Ferraro (1992), independently pointed out that a proper inclusion of the α -element enhancement in the computation of the global metallicity of the parent cluster could reduce the discrepancy. In a recent review of the problem, Cassisi & Salaris (1997) essentially re-obtained the same result.

Since the early work presented in F90, the RGB-Bump has been identified in a growing number of GGCs (see for example Brocato et al. 1996). As pointed out by Rood & Crocker (1985), the best tool to identify the RGB-bump is the Luminosity Function (LF), and both the integrated and the differential LFs are useful (Ferraro 1992). Following the prescriptions of F90 we independently identified the RGB-bump in 47 GGCs in our catalog. The bump magnitudes so measured are listed

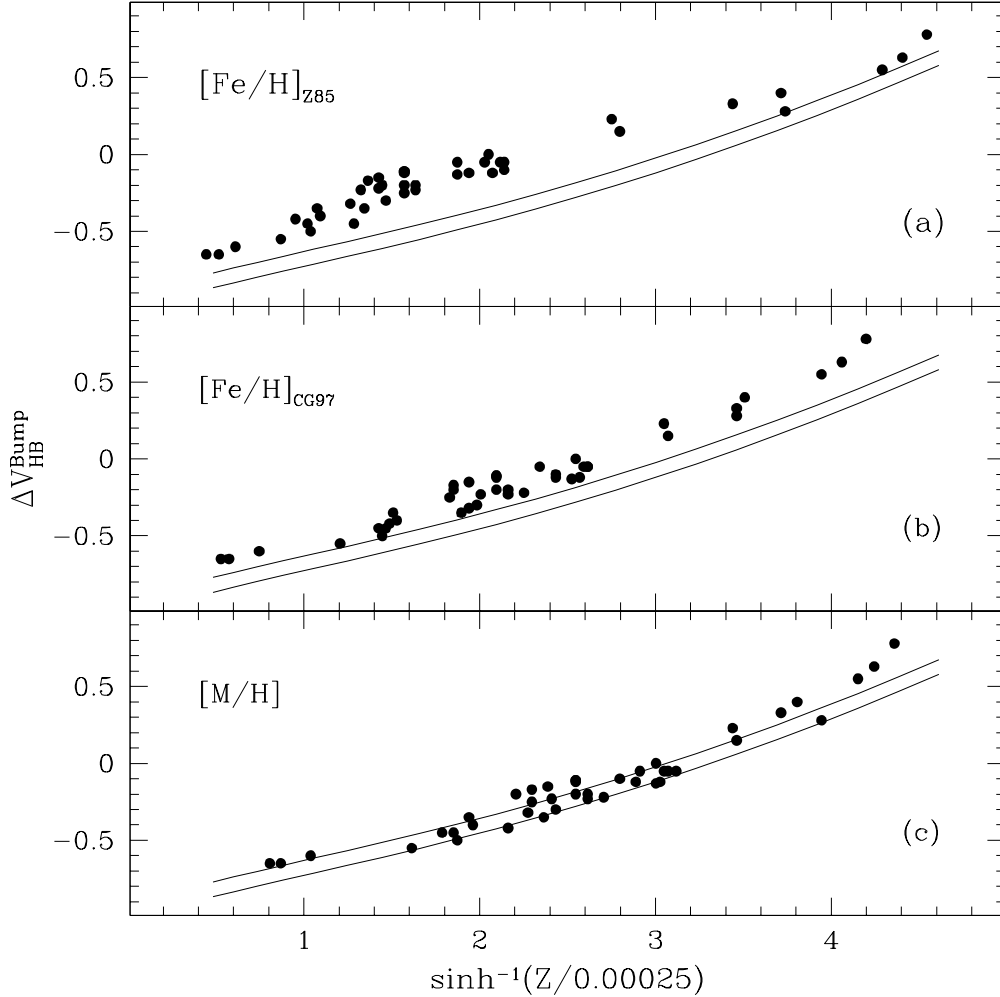


Fig. 14.— The same as Figure 12 for the three different metallicity scales: Zinn 1985 (upper panel), Carretta & Gratton 1997 (central panel), *global* metallicity $[M/H]$ (lower panel). The two solid line represent the theoretical predictions for two different ages, namely 12 (lower line) and 16 Gyr (upper line).

in column 5 of Table 5. This represents the largest GGCs sample listing the RGB-bump locations available so far.

To allow comparisons with both previous studies and theoretical models, following F90, we have measured the parameter: $\Delta V_{HB}^{Bump} = V_{Bump} - V_{HB}$, which has the advantage of being actually independent of the photometric zero-point of the cluster data, the reddening, and the distance

modulus. Moreover we have also adopted the parameter s defined as: $s = \sinh^{-1}(Z/0.00025)$, where $Z = 10^{[\text{Fe}/\text{H}]-1.7}$. This quantity is best suited to linearly describe the dependence of $\Delta V_{\text{HB}}^{\text{Bump}}$ on metallicity (F90).

As a starting point, we first adopt the same metallicity scale as F90, namely the Zinn (1985) scale. In Figure 12a, we reported the $\Delta V_{\text{HB}}^{\text{Bump}}$ as a function of $[\text{Fe}/\text{H}]$, while in Figure 12b the same quantity is plotted versus s . As can be seen there is a clearcut correlation. The error bars, as expected, tend to be systematically larger at lower metallicities, due to the difficulty, mentioned above, in identifying the bump in those GGCs.

The best fit to the data obtained by F90 is also overplotted to the new values in the same figure. As can be seen there is a systematic shift, the new values being slightly lower than the old ones by about 0.05-0.1 mag. Such a difference is mainly due to the new procedure used to measure the ZAHB level. In fact in F90 the lower edges of the observed HB distributions were assumed to be coincident with the ZAHB levels (see the discussion presented in section 4).

On the theoretical side, the latest models which include improvements in the input physics imply a reduction of the predicted luminosity level of the RGB bump (see e.g. table 4 in SCL97). In addition to that, larger core masses at the He flash are now obtained, so that the predicted HB luminosity is larger than those found in the old computations. On the base of the RGB and HB models described in Section 4, we have derived the following relation for the RGB-bump location:

$$M_V^{\text{Bump}} = 0.7502 + 0.9896 \log t_9 + 1.5797[\text{M}/\text{H}] + 0.2574[\text{M}/\text{H}]^2 \quad (3)$$

where t_9 is the age in Gyr, and for the ZAHB level:

$$M_V^{\text{ZAHB}} = 1.0005 + 0.3485[\text{M}/\text{H}] + 0.0458[\text{M}/\text{H}]^2 \quad (4)$$

In order to make easy the comparison with other published relation for the ZAHB level as a function of the metallicity, it could be useful to give here also the linear best-fit regression in the range $-0.4 < [\text{M}/\text{H}] < -2.2$:

$$M_V^{\text{ZAHB}} = 0.23[\text{M}/\text{H}] + 0.94 \quad (5)$$

In Figure 13 we show a comparison between the old theoretical values (adopted by F90) for the $\Delta V_{\text{HB}}^{\text{Bump}}$ parameters and the latest ones. The new values are significantly larger by about 0.15–0.20 mag (up to 0.3 mag at the largest metallicity). Results from the new models are compared to the present data in Figure 14. We show the theoretical expectations for two different ages, 12 and 16 Gyr, which are roughly representative of the range of ages covered by the bulk of the Galactic Globular Clusters. The “old” (Z85) and the “new” (CG97) metallicity scale are shown, in panel a) and b) respectively. Finally in panel c) we adopt the *global* metallicity ($[\text{M}/\text{H}]$). Note that only in this third case a good agreement between the theory and the observations is obtained. The previous discrepancy of about 0.4 mag between theory and observation has been completely removed. The major changes are:

- The updated input physics in the evolutionary models which yields: RGB bump less luminous (by $\sim 0.1-0.15$ mag) because of the increased opacity, and HB level more luminous (by ~ 0.05 mag) because of increased core mass.

- The new spectroscopic abundances ($[\alpha/\text{Fe}]$ and $[\text{Fe}/\text{H}]$) which contribute ~ 0.2 mag.
- The new definition of the HB level, which contributes $\sim 0.05 - 0.1$ mag.

The best fit relations obtained in terms of the different metallicity scales are listed in Table 6. For each metallicity scale the behaviour of the $\Delta V_{\text{HB}}^{\text{Bump}}$ parameter has been computed both in terms of the usual metallicity parameter ($[\text{Fe}/\text{H}]$, $[\text{M}/\text{H}]$ etc) and the parameter s defined by F90.

7. THE ASYMPTOTIC GIANT BRANCH

According to the evolutionary models (Castellani, Chieffi & Pulone, 1991), after the exhaustion of the central He, the He-burning rapidly move from the center toward the maximum mass coordinate attained by the convective core during the HB phase. Thus, the beginning of the AGB is characterized by a rapid increase of the luminosity. When the shell He burning stabilizes, a slowing down in the evolutionary rate is expected. Then, from an observational point of view, the transition between the central and the shell He-burning should be marked by a clear gap (where few stars should be found), while a well defined clump of stars should indicate the base of the AGB.

It has been recognized (Castellani, Chieffi & Pulone 1991, Pulone 1992, Bono et al. 1995) that the luminosity level of the AGB-clump is almost independent of the chemical composition of the cluster stars (both Z and Y), so that this (quite bright) feature could be a very promising “standard candle.” However, we note that the theoretical calibration of the AGB clump location is affected by the uncertainties in the actual extension of the convective core of an He burning low mass stars. On the other hand, as pointed out by Caputo et al. (1989) one might use the observed differences between the HB luminosity level and that of the AGB-clump (i.e. $\Delta V_{\text{AGB}}^{\text{HB}} = V_{\text{clump}}^{\text{AGB}} - V_{\text{HB}}$) to constrain the convection theory (instability criterion, semiconvection, overshooting and the like; see Dorman & Rood 1993).

Unfortunately, the identification of such a clump is not easy since the AGB phase itself is very short ($\sim 10^7$ yr) and, in turn, always poorly populated (a GGC with total luminosity $L_T = 10^5 L_{\odot}$ contains ~ 20 AGB stars; see Renzini & Fusi Pecci 1988). There are a few identifications of the AGB-clump in the literature: Ferraro (1992) reported a preliminary identification of this feature in 3 GGCs (M5, NGC 1261, NGC 2808), and Montegriffo et al (1995) showed that it is clearly visible in 47 Tuc. Other examples could be found in published CMD’s, but the AGB-clump detection has neither been noted nor discussed.

To initiate a systematic study of the properties of the AGB-clump, we have independently identified such a feature in 9 GGCs whose CMDs show a significant clump of stars in the AGB region. In Table 5 (column 6), the apparent V magnitudes of the approximate centroid of the AGB-clump stars distribution are listed for each of these 9 clusters.

In order to study the behaviour of the AGB-clump from a theoretical point of view, a subset of CLS98 models were continued through the onset of He shell burning up to the the of the first thermal pulse. The main results are presented in Figure 15 where the absolute V magnitude of the AGB-clump is plotted versus the ZAHB mass, for two different metallicities ($\log Z = -3$ and $\log Z = -4$, respectively). The corresponding $(B - V)$ colours of the AGB-clump are also reported for each model. Both the colour and the luminosity of the AGB-clump depend significantly on the stellar mass (see also Fig 2 by Castellani, Chieffi & Pulone 1989).

Table 5. RGB and AGB Bump parameters.

<i>Name</i>	[Fe/H] _{CG97}	[M/H]	V_{ZAHB}	V_{RGB}^{Bump}	V_{AGB}^{Bump}
NGC 104	-0.70	-0.59	14.22±0.07	14.55±0.05	13.15±0.07
NGC 288	-1.07	-0.85	15.50±0.10	15.45±0.05	—
NGC 362	-1.15	-0.99	15.50±0.07	15.40±0.10	—
NGC1261	-1.09	-0.89	16.72±0.05	16.60±0.05	15.65±0.05
NGC1466	-1.64	-1.44	19.30±0.07	—	—
NGC1841	-2.11	-1.91	19.42±0.10	—	18.55±0.10
NGC1851	-1.08	-0.88	16.20±0.05	16.15±0.05	—
NGC1904	-1.37	-1.22	16.27±0.07	15.95±0.05	—
NGC2419	-1.97	-1.77	20.50±0.10	—	—
NGC2808	-1.15	-0.95	16.27±0.07	16.15±0.05	15.20±0.07
NGC3201	-1.23	-1.03	14.77±0.07	14.55±0.05	—
NGC4147	-1.58	-1.38	16.95±0.10	—	—
NGC4372	-1.94	-1.74	15.90±0.15	—	—
NGC4590	-1.99	-1.81	15.75±0.05	15.15±0.05	—
NGC4833	-1.58	-1.27	15.77±0.07	15.35±0.05	—
NGC5053	-2.51	-2.31	16.70±0.07	—	—
NGC5272	-1.34	-1.16	15.68±0.05	15.45±0.05	14.80±0.05
NGC5286	-1.57	-1.37	16.60±0.10	16.25±0.05	15.57±0.10
NGC5466	-2.14	-1.94	16.62±0.10	—	—
NGC5694	-1.72	-1.52	18.70±0.10	18.15±0.07	—
NGC5824	-1.64	-1.44	18.52±0.07	—	—
NGC5897	-1.59	-1.44	16.45±0.07	16.00±0.10	—
NGC5904	-1.11	-0.90	15.13±0.05	15.00±0.05	14.15±0.05
NGC5927	-0.46	-0.37	16.72±0.10	—	—
NGC6093	-1.41	-1.21	16.12±0.07	15.95±0.10	—
NGC6121	-1.19	-0.94	13.45±0.10	13.40±0.10	—
NGC6171	-0.87	-0.70	15.70±0.10	15.85±0.05	—
NGC6205	-1.39	-1.18	15.10±0.15	14.75±0.07	—
NGC6218	-1.37	-1.17	14.75±0.15	14.60±0.07	—
NGC6229	-1.30	-1.10	18.11±0.05	18.00±0.07	17.15±0.05
NGC6254	-1.41	-1.25	14.85±0.10	14.65±0.05	—
NGC6266	-1.07	-0.87	16.40±0.20	16.35±0.05	—
NGC6333	-1.56	-1.36	16.35±0.15	15.95±0.10	—
NGC6341	-2.16	-1.95	15.30±0.10	14.65±0.05	—
NGC6352	-0.64	-0.50	15.30±0.10	—	—
NGC6366	-0.87	-0.70	15.80±0.10	—	14.75±0.10
NGC6397	-1.82	-1.65	13.00±0.10	—	—
NGC6440	-0.49	-0.40	18.70±0.20	19.25±0.05	—
NGC6528	-0.38	-0.31	17.17±0.20	17.95±0.10	—
NGC6535	-1.53	-1.33	15.90±0.15	—	—

Table 5—Continued

<i>Name</i>	[Fe/H] _{CG97}	[M/H]	V_{ZAHB}	V_{RGB}^{Bump}	V_{AGB}^{Bump}
NGC6553	-0.44	-0.36	16.92±0.20	17.55±0.10	—
NGC6584	-1.30	-1.10	16.60±0.05	16.40±0.10	—
NGC6637	-0.68	-0.55	15.95±0.10	16.35±0.07	—
NGC6652	-0.87	-0.70	16.07±0.10	—	—
NGC6681	-1.27	-1.07	15.85±0.10	15.65±0.05	—
NGC6712	-0.88	-0.71	16.32±0.07	16.55±0.05	—
NGC6717	-1.10	-0.90	15.75±0.15	15.75±0.10	—
NGC6752	-1.42	-1.21	13.90±0.15	13.65±0.05	—
NGC6809	-1.61	-1.41	14.60±0.10	14.15±0.05	—
NGC6838	-0.70	-0.49	14.52±0.10	14.80±0.15	—
NGC6934	-1.30	-1.10	16.97±0.07	16.85±0.05	—
NGC6981	-1.30	-1.10	16.86±0.07	16.75±0.07	—
NGC7006	-1.35	-1.15	18.85±0.15	18.55±0.07	—
NGC7078	-2.12	-1.91	15.90±0.07	15.25±0.05	—
NGC7099	-1.91	-1.71	15.30±0.10	—	—
NGC7492	-1.27	-1.07	17.78±0.10	17.55±0.10	—
IC4499	-1.26	-1.06	17.70±0.07	—	—
Rup 106	-1.70	-1.50	17.85±0.10	—	—
Arp 2	-1.64	-1.44	18.30±0.15	—	—
Ter 7	-0.64	-0.52	17.87±0.10	—	—
Ter 8	-1.60	-1.40	18.15±0.10	17.65±0.10	—

In particular higher stellar masses tend to generate brighter and redder AGB clump. Thus, in principle, the dependence of the AGB-clump luminosity on the mass of the evolving star implies, in turn, an indirect dependence on all the other parameters which could affect the mean mass (and its distribution) along the HB: namely metallicity, age, mass loss efficiency and all the parameters which directly or indirectly affect the mass loss process. However, it is interesting to note that for low metallicity clusters (but in general for clusters with blue HB) the AGB clump rapidly tends to become bluer and bluer (up to $(B - V) \sim 0.0$) and probably (due to the spread in mass along the ZAHB) progressively less *clumpy* and, for this reason, less observable. This effect is nicely shown, for example, by Fig 4 in Rood, Whitney & D’Cruz 1997 and Fig. 8 in Whitney et al. (1998). Thus, operatively, whether the AGB clump is observable or not determines to some extent the possible range luminosity which might be observable for this feature. The models suggest that observable AGB-Bumps are located at $M_V^{\text{AGB-Bump}} = -0.3 \pm 0.1$

In Figure 16, we compare the theoretical and observed values of the $\Delta V_{\text{HB}}^{\text{AGB}}$ parameter. The shaded region represents the quoted uncertainty (± 0.1) in the absolute location of the AGB clump. Despite the quite large error bar affecting most of the (few) available measurements of the AGB-

Table 6. RGB-Bump parameters and their calibration in terms of the different metallicity scales.

The Zinn Scale $[\text{Fe}/\text{H}]_{Z85}$		
$\Delta V_{\text{HB}}^{\text{Bump}} = 0.31s_{Z85} - 0.72$	n=42 $\sigma = 0.07$	(6.1)
$\Delta V_{\text{HB}}^{\text{Bump}} = 0.67[\text{Fe}/\text{H}]_{Z85} + 0.827$	n=42 $\sigma = 0.06$	(6.2)
The Carretta-Gratton Scale $[\text{Fe}/\text{H}]_{\text{CG97}}$		
$\Delta V_{\text{HB}}^{\text{Bump}} = 0.041s_{\text{CG97}}^2 + 0.172s_{\text{CG97}} - 0.753$	n=42 $\sigma = 0.06$	(6.3)
$\Delta V_{\text{HB}}^{\text{Bump}} = 0.269[\text{Fe}/\text{H}]_{\text{CG97}}^2 + 1.451[\text{Fe}/\text{H}]_{\text{CG97}} + 1.220$	n=42 $\sigma = 0.06$	(6.4)
The <i>global</i> Scale $[\text{M}/\text{H}]$		
$\Delta V_{\text{HB}}^{\text{Bump}} = 0.065s_{\text{global}}^2 + 0.025s_{\text{global}} - 0.702$	n=42 $\sigma = 0.07$	(6.5)
$\Delta V_{\text{HB}}^{\text{Bump}} = 0.360[\text{M}/\text{H}]^2 + 1.602[\text{M}/\text{H}] + 1.113$	n=42 $\sigma = 0.07$	(6.6)
The Bump location in the absolute plane M_V^{Bump}		
$M_V^{\text{Bump}} = 0.29[\text{Fe}/\text{H}]_{\text{CG97}}^2 + 1.736[\text{Fe}/\text{H}]_{\text{CG97}} + 2.23$	n=42 $\sigma = 0.06$	(6.7)
$M_V^{\text{Bump}} = 0.406[\text{M}/\text{H}]^2 + 1.95[\text{M}/\text{H}] + 2.113$	n=42 $\sigma = 0.06$	(6.8)

clump, the level of the agreement with the theoretical prediction is remarkable. Such a result, especially combined with that obtained in Section 6.4 for the RGB-bump location, is comforting about the reliability and the internal consistency of the adopted theoretical prescriptions.

For sake of completeness we give below the best fit relation of the $\Delta V_{\text{HB}}^{\text{AGB}}$ parameter as a function of the metallicity in the CG97 and *global* metallicity scale, respectively:

$$\Delta V_{\text{HB}}^{\text{AGB}} = -0.16[\text{Fe}/\text{H}]_{\text{CG97}} - 1.19 \quad (n = 9, \sigma = 0.06) \quad (6)$$

$$\Delta V_{\text{HB}}^{\text{AGB}} = -0.17[\text{M}/\text{H}] - 1.17 \quad (n = 9, \sigma = 0.05) \quad (7)$$

8. TOWARDS ABSOLUTE QUANTITIES

In order to carry out an exhaustive comparison with the models we have to derive *absolute* quantities from our data. This implies the knowledge (or the assumption) of a “reliable” distance scale for the program clusters. As it is well known (see for instance the recent discussion by Gratton

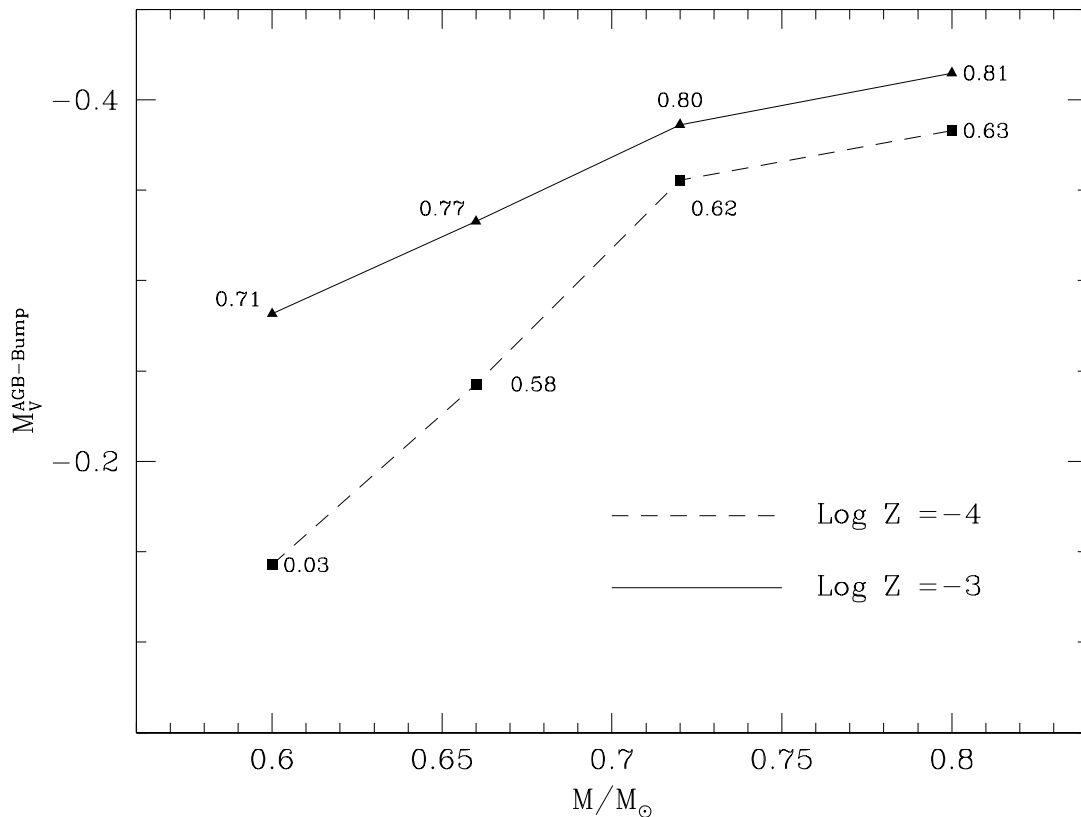


Fig. 15.— The theoretical luminosity level of the AGB clump as function of the stellar mass for two metallicities, namely $Z=0.0001$ and $Z=0.001$ (dashed and solid line, respectively). The labels reported in the figure are the B-V colours of the computed AGB clumps.

et al 1997, and Carretta et al 1999, hereafter C99) different loci in the CMD and different standard candles can be assumed to determine the distance to a given cluster (see also Cacciari 1998 for an extensive review). Here we adopt just *a given* standard candle, and briefly comment on the possible impact of alternative choices. Any variation of the zero-point or of the metallicity dependence of the luminosity of the adopted candles would in fact affect the conclusions.

Since our study is mainly devoted to the quantitative analysis of the evolved sequences (including the HB), it is quite natural to adopt HB stars as standard candles, at least for heuristic purposes. Unfortunately, although the HB is the *classical* sequence traditionally used as refer-

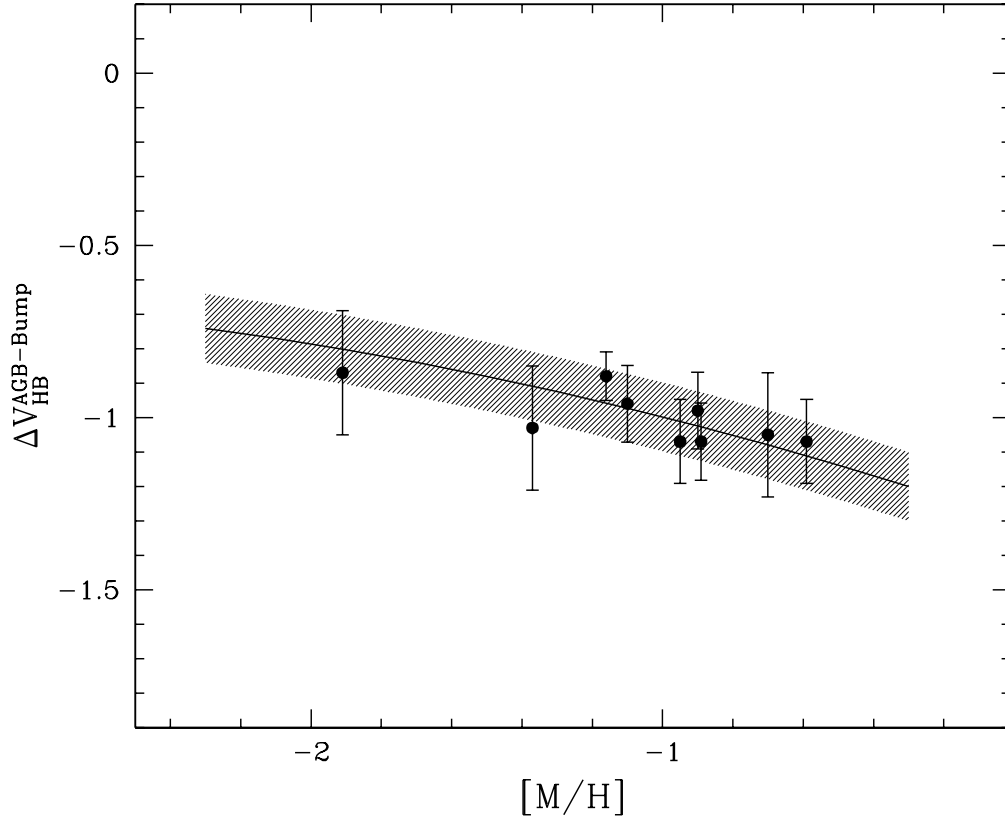


Fig. 16.— The difference between the observed ZAHB and AGB clump luminosity levels of 9 clusters in our catalog. The solid line is the theoretical expectation. The dashed region is representative of the uncertainty (± 0.1 mag) in the absolute location of the AGB-clump (see text).

ence branch, there is still strong disagreement on the basic *absolute* calibration. For the sake of discussion, in the following we will use our theoretical ZAHB as standard candles, as this choice guarantees a complete self-consistency in our approach. We leave to future studies the assessment of the validity of the HB-models as suitable candles. We discarded here the use of empirical relations since none of those presented so far (see for references Vandenberg, Stetson & Bolte, 1996, Gratton et al. 1997, Reid 1997, 1998, Cacciari 1998) actually calibrate the “true” ZAHB-level but rather adopt the mean apparent magnitude of the HB at a given color, $\langle V_{\text{HB}} \rangle$, or an empirically derived ZAHB level, obtained from the mean HB level via some metallicity and HB morphology dependent correction factors.

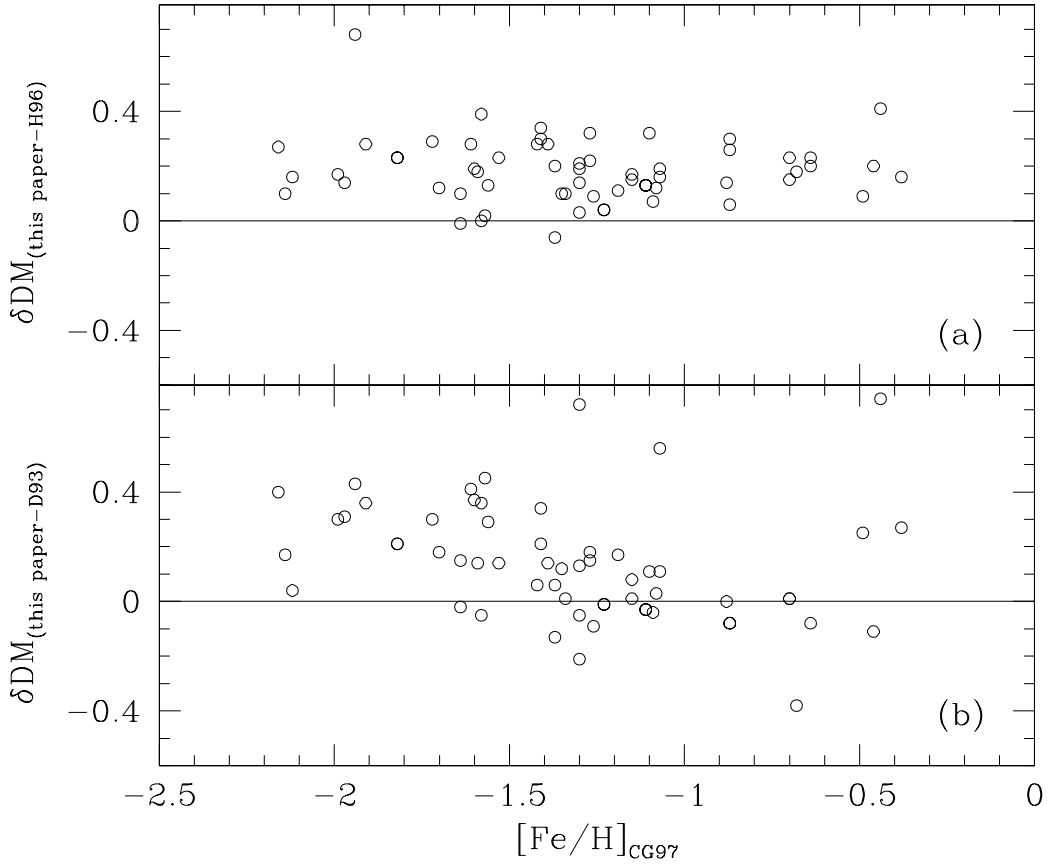


Fig. 17.— Difference between the DM obtained in this paper and the previous compilations by H96 and D93 (*panel (a)* and *(b)*, respectively). A systematic difference of ~ 0.2 mag is evident in the comparison with H96 data. The trend with the metallicity clearly evident in *panel (b)* is due to the D93 assumption on the $V(HB)$, (see text).

The distance moduli were computed by adopting as reference equation (4) of section 6.4. Values were computed using both the metallicity scale from the spectroscopic iron abundance measurements (GC97) and the global metallicity scale (as derived in Section 3). Note that the

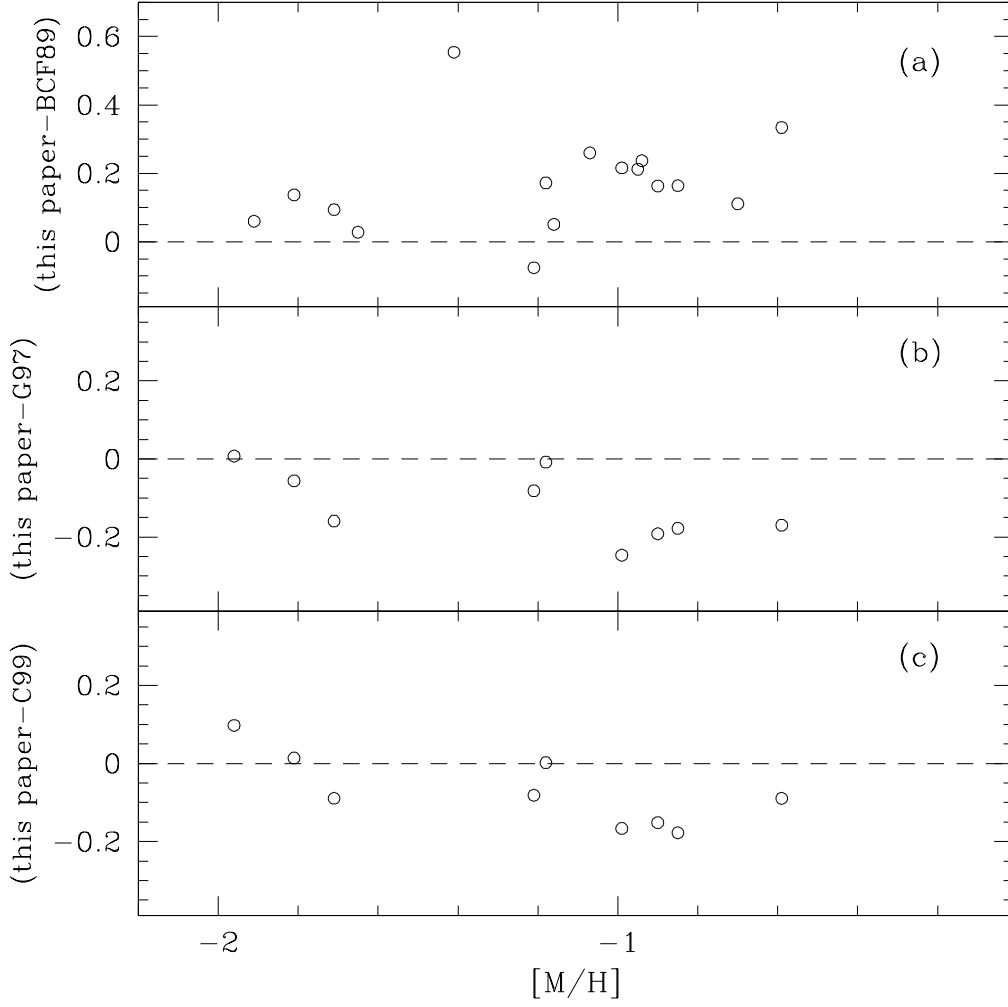


Fig. 18.— Difference between the DM obtained in this paper and those obtained from: *panel (a)* BCF89; *panel (b)* Hipparcos parallaxes (Gratton et al 1997); *panel (c)* Revised Hipparcos parallaxes (Carretta et al 1999).

adoption of the CG97 spectroscopic scale rather than the Z85 leads to an average decrease of the absolute luminosity of the ZAHB level and, in turn, of the derived distance scale by ~ 0.03 . An additional decrease in luminosity (~ 0.04 mag) occurs if α -enhancements are included to get the global metallicity ($[M/H]$).

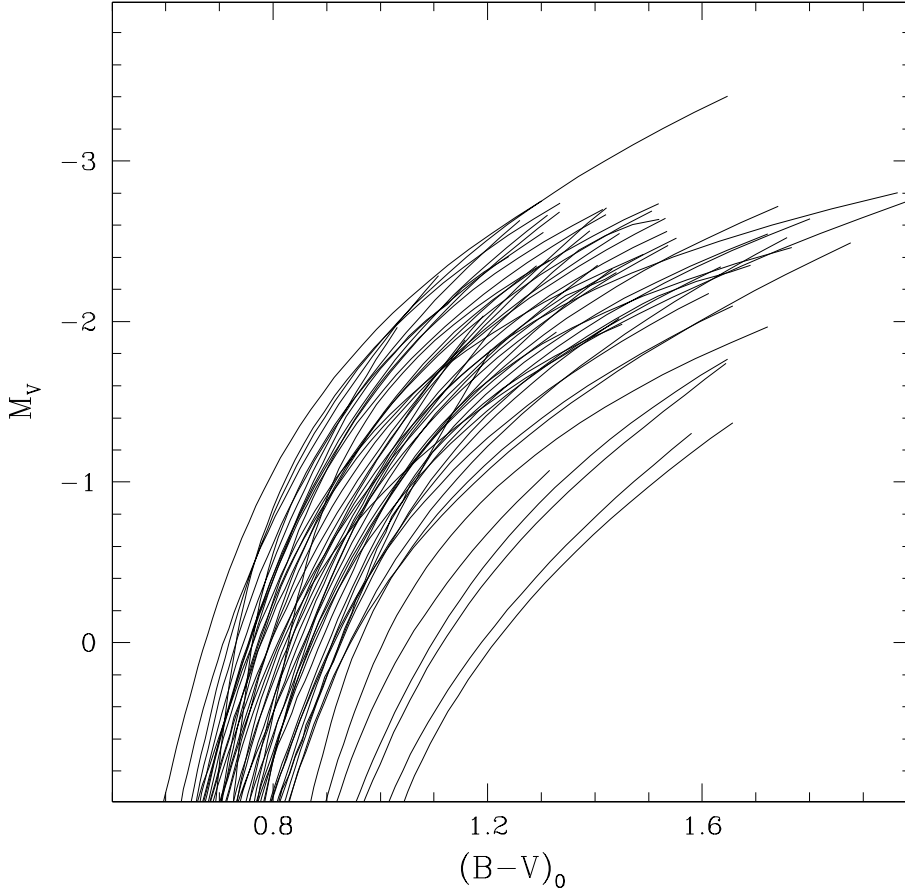


Fig. 19.— RGB mean ridge lines for 55 GGCs in the absolute plane (M_V , $(B-V)_0$). The adopted DM as been computed assuming the metallicity in the CG97 scale (see text).

The distance moduli obtained assuming $[\text{Fe}/\text{H}]_{\text{CG97}}$ and $[\text{M}/\text{H}]$ are listed in Table 2, column 7 and 8, respectively. Note that in computing the DM we adopted the individual reddening as listed in column 5 of Table 2. Considering that the derived DM are affected by many uncertainties (namely, the evaluation of the ZAHB level, the zero point and dependence on metallicity of the ZAHB level, reddening, etc) we estimate that the global uncertainty affecting the DM listed in Table 2 cannot be less than 0.2 mag.

These values can be then compared with those reported in the two most recent compilations of GGC observable parameters: Djorgovski (1993) and Harris (1996), respectively, which were, however, derived under assumptions significantly different from those adopted here. In fact, Djorgovski (1993) assumed a constant value for the HB level ($M_V^{\text{HB}} = 0.6$) independent of metallicity, while Harris (1996) adopted $M_V^{\text{HB}} = 0.20[\text{Fe}/\text{H}] + 1.0$, based on the empirical relation obtained by

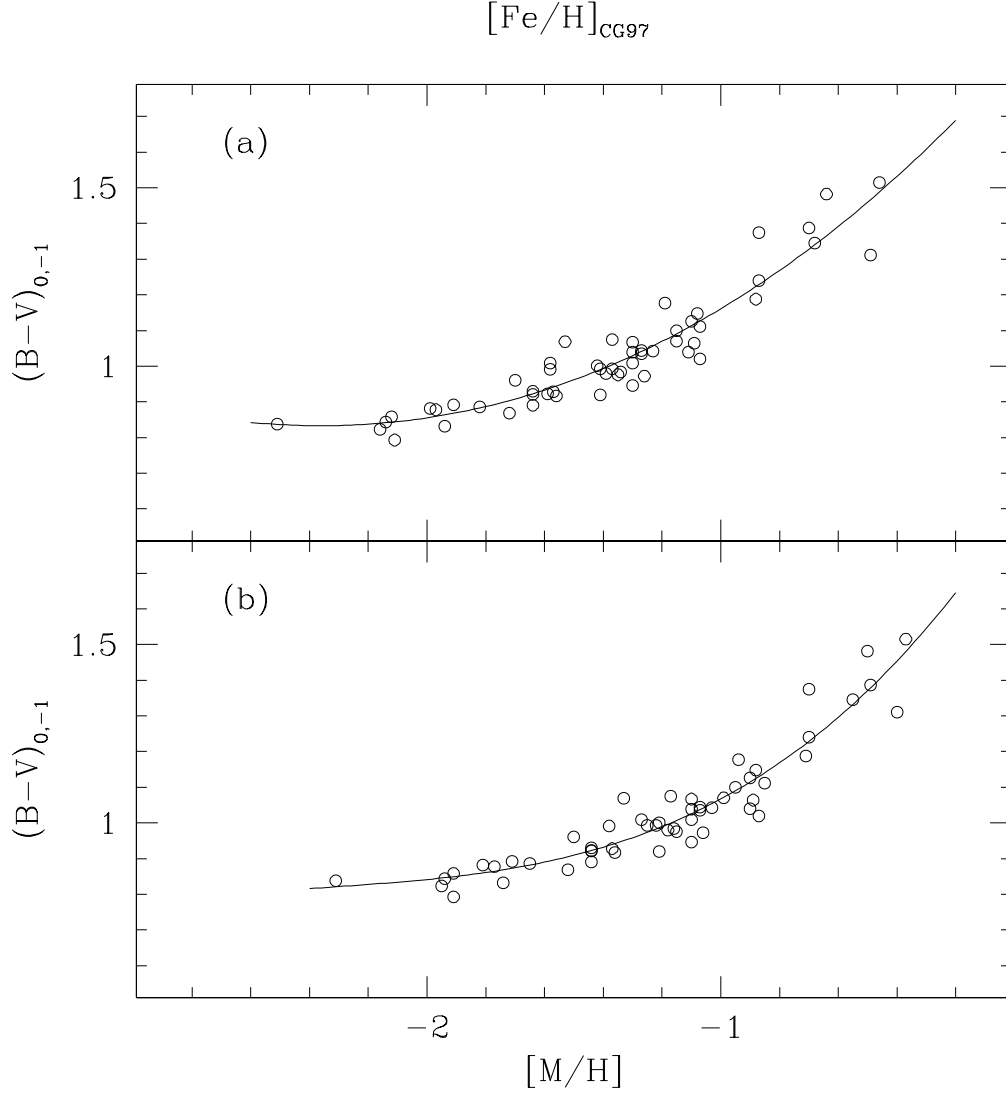


Fig. 20.— Intrinsic $(B - V)_0$ colour of the RGB, measured at $M_V = -1$ as function of $[Fe/H]_{CG97}$ and $[M/H]$, *panel (a)* and *(b)*, respectively. The solid lines are the best fit relations listed in Table 4 (relation 4.15 and 4.16, respectively).

Carney, Storm & Jones (1992).

The residuals for the DM (this – previous paper) as a function of $[Fe/H]_{CG97}$ are plotted in Figure 17a,b, for D93 and H96, respectively. In the comparison with D93 there is a clear trend of the residuals as a function of metallicity, mostly due to the assumption of a constant M_V^{HB} . No similar

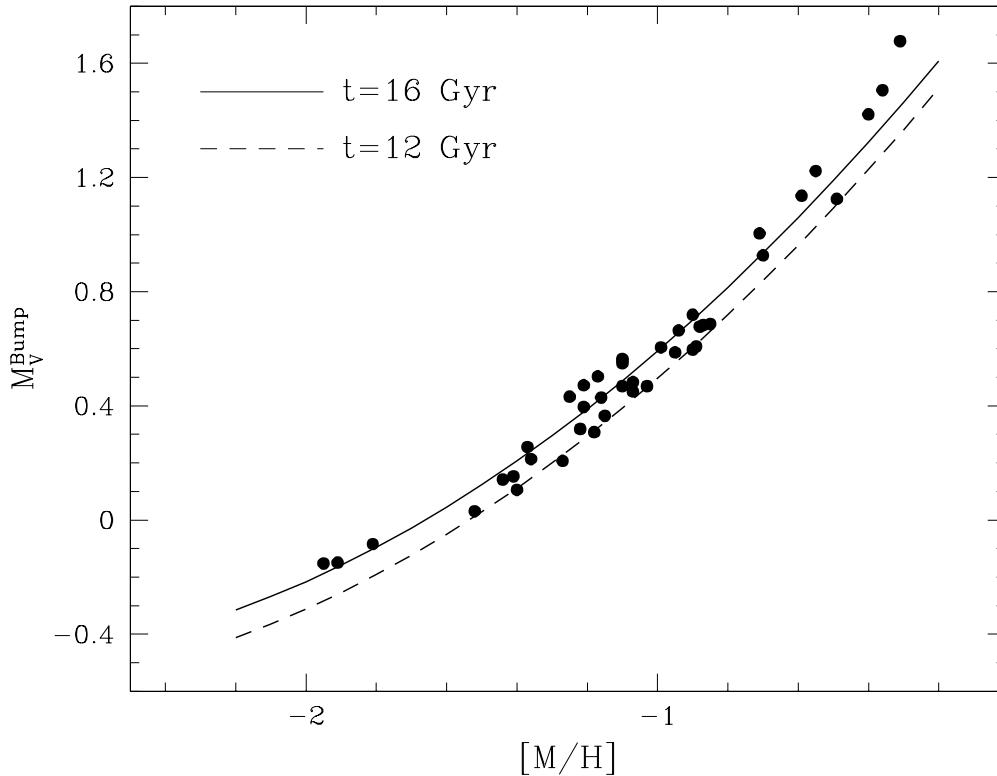


Fig. 21.— The absolute magnitude of the RGB Bump as a function of the global metallicity $[M/H]$ (the DM has been computed accordingly). The solid line is the theoretical prediction by CLS98 models at $t=16$ Gyr, the dashed line represent the same set of models at $t=12$ Gyr.

trend is detectable with respect to H96, since the assumption on the slope of the $M_V(HB) - [Fe/H]$ relation is compatible with the one assumed here (see eq. 5). There is however a clear systematic offset ($\sim 0.15 - 0.2$) partially due to the different zero-point of the adopted relation and partially due to the difference in the procedure used to determine level of the ZAHB (see Section 5).

8.1. Comparison with other empirical distances

As quoted in the previous section an extensive comparison between the distance moduli obtained here and those derived adopting different standard candles is beyond the purpose of the present paper. For sake of example in this section we report two among the most recent results obtained adopting different candles.

8.1.1. The Main Sequence

Among others, this approach was used by BCF89 who compared the observed MS mean ridge lines for a sample of 19 GGCs with the *reference* locus defined by 6 local subdwarfs. From this procedure they derived distances and ages for the program clusters. The residuals of the comparison of the DM (this paper – BCF89) are plotted as a function of metallicity ($[\text{Fe}/\text{H}]_{\text{CG97}}$) in Figure 18a. As can be seen the mean difference is ~ 0.15 mag, the DM derived in this paper being systematically larger than those obtained by BCF89. The discrepancy (~ 0.6) found for NGC 6809 is due in part to the different photometry adopted here and in part to the different assumption on the reddening: BCF89 assumed 0.14 while here we used 0.07 from Harris 1996).

The same methodological approach has been followed recently by Gratton et al (1997), who gave new distances for a sample of 9 GGCs. These distances are based on high precision trigonometric parallaxes for a sample of ~ 30 local subdwarf from the HIPPARCOS satellite. They found that the derived distances for the selected sample of GGCs are systematically larger (~ 0.2 mag) than previously estimated. The residuals of the corresponding distances (this paper – Hipparcos) are plotted as a function of metallicity ($[\text{Fe}/\text{H}]_{\text{CG97}}$) in Figure 18b. While there is agreement between our DM and the HIPPARCOS DM at the lowest metallicities, there seems to be a systematically increasing discrepancy as metallicity increases. The sample is certainly too poor to derive any firm conclusion.

However it is interesting to note that the recent re-analysis of the HIPPARCOS data presented by C99 goes in the direction of showing a better agreement with the distances obtained in this paper; in Figure 17c, the residuals with respect to these most recent determinations have been plotted, as can be seen from the figure the distances determinations for clusters in the low-metallicity domain nicely agree, while some systematic difference still remain at the high-metallicity end. Since the difference on the distance modulus of about 0.07 mag implies a corresponding difference in age of about 1 Gyr, it is quite evident that the differences found for specific cluster are still high as far as the age determination is concerned. However the sample is so small that it is still impossible to draw any reliable conclusion.

It is also important to bear in mind that due to the steepness of the MS the “main sequence fitting” method to derive distances is strongly limited by any uncertainty affecting the MS colours (metallicity, reddening, photometry calibration and the like) of both the clusters and the reference stars (subdwarfs).

8.1.2. White Dwarfs

The cooling sequence of white dwarfs has been used recently by Renzini et al (1996) as a distance indicator to determine the distance of the nearby cluster NGC 6752. For this cluster they derived $(m - M)_0 = 13.05$ with an overall uncertainty of ± 0.1 mag. This value is compatible with the DM obtained using the global metallicity ($[\text{M}/\text{H}]$) $(m - M)_0 = 13.14 \pm 0.10$ (see column 8 in Table 2).

8.2. The absolute quantities

Using the assumptions and results obtained in the previous sections for the distances, it is possible to obtain various interesting plots which describe in a very direct and clear way the properties of the RGB (and in particular its location and morphology) with varying metallicity.

In Figure 19, we present the mean ridge line for 55 GGCs in the absolute plane ($M_V, (B-V)_0$). The DM obtained from the $[\text{Fe}/\text{H}]_{\text{CG97}}$ scale have been adopted to construct the diagram. As can be noted by this figure at least three clusters (namely NGC6333, NGC6535, NGC7492) appear to cross over the other mean ridge lines suggesting that photometries for these clusters could be affected by calibration problems and they deserve a more accurate photometric analysis.

Figure 20a,b report the intrinsic colours of the RGB measured at $M_V = -1$ (labelled as $(B-V)_{0,-1}$ and listed in column 10 of Table 3) as a function of $[\text{Fe}/\text{H}]_{\text{CG97}}$ and $[\text{M}/\text{H}]$, respectively. Also plotted are the best fit relations reported in Table 4 (eq. 4.15 and 4.16).

Figure 21 shows the dependence of the absolute location of the RGB-Bump on the global metallicity. For comparison with theoretical expectation, the relation by SCL97 has been overplotted at two different ages (as in the previous figure), at 16 Gyr (the solid line) and 12 Gyr (the dashed line). As can be seen from this figure the previous discrepancy between the observation and the model prediction for the location of this feature is completely removed using the new models and considering the global metallicity scale (as expected from the discussion in Section 6.4). Finally analytic relations giving the absolute magnitude of the RGB-Bump as a function of the metallicity using both the CG97 and *global* scale have been computed. They are listed in Table 5 (relations 5.7 and 5.8).

Though intriguing in principle, the uncertainty on the data is still too large to allow any attempt to derive informations on a possible age spread within the GGCs system from such a data-set.

9. FINAL REMARKS ON THE METALLICITY ASSUMPTIONS

In this section we briefly discuss the effects of adopting different assumptions for the metallicity on the relations we derived in the previous sections. In particular:

(i) the use of the metal abundance ($[\text{Fe}/\text{H}]$) estimates obtained by RHS97 in the CG97 scale instead of those listed in column 3 of Table 1;

(ii) the adoption of the Carney (1996) scenario for the α -element enhancing relation (see Figure 2b), rather than that one plotted in Figure 2a, in computing the global metallicity.

(i) As already shown in Figure 1b the metal abundance obtained by RHS97 in the CG97 scale for the 42 GGCs in common is fully compatible (within 0.2 dex) with that one adopted in this paper (computed following the procedure described in Section 3.2). For this reason we expect very small effect on the relations we derived in the previous Sections. For sake of example in Figure 22 we report the results for the relations we obtained for three of the RGB parameters we defined in Section 6.2 (namely $S_{2.0}$, $\Delta V_{1.2}$, $(B-V)_{0,g}$). On the left panels of Figure 21 we plotted the relations obtained assuming $[\text{Fe}/\text{H}]_{\text{CG97}}$ listed in Table 1, in the right panels those assuming the values listed by RHS97. The number of the clusters used to compute each relation is shown in each panel together with the standard deviation of the data. In order to properly compare the scatter of

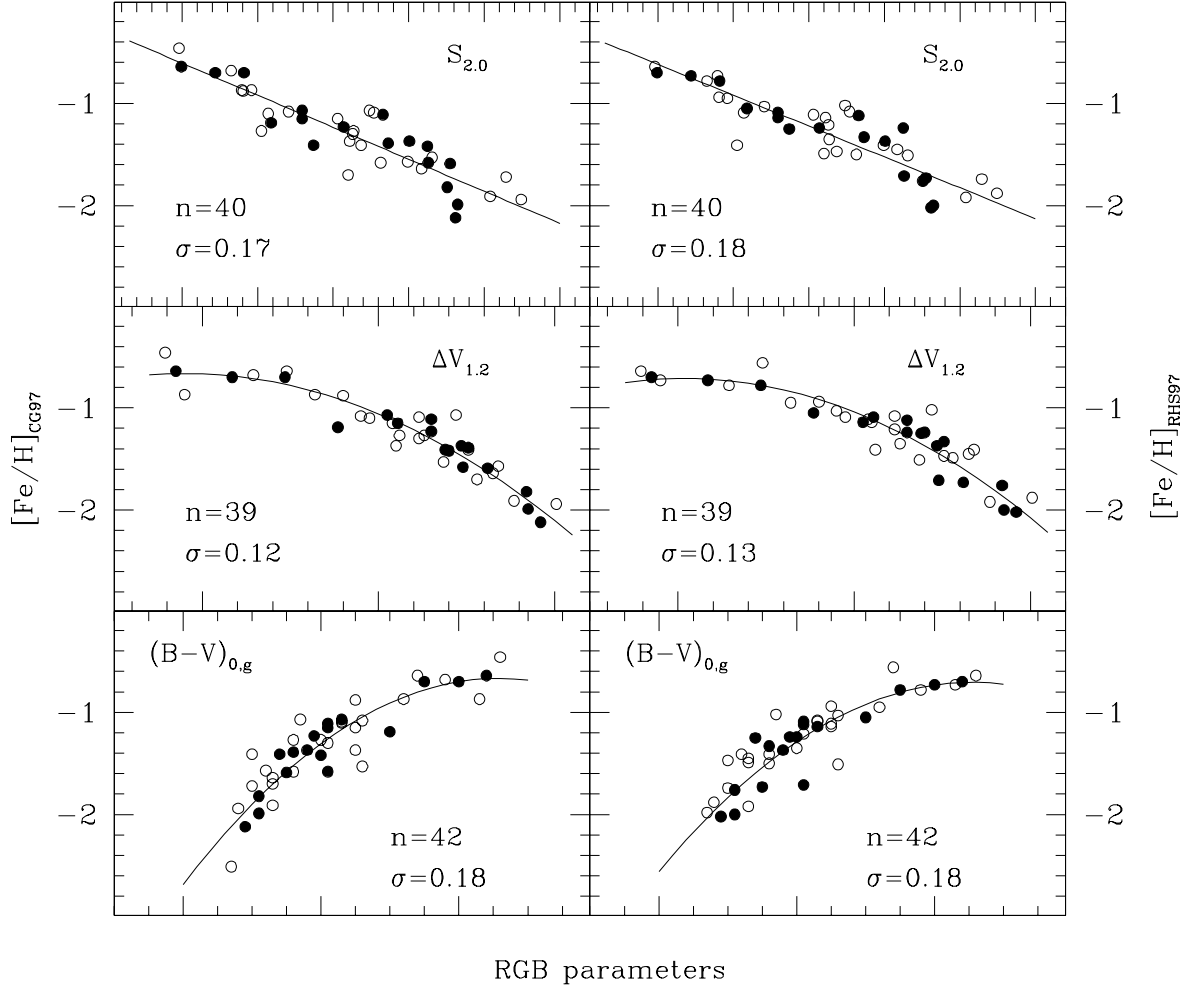


Fig. 22.— $[Fe/H]_{CG97}$ versus the values obtained for three RGB parameters defined in Section 6.2 (namely $S_{2.0}$, $\Delta V_{1.2}$, $(B-V)_{0,g}$) as computed in Section 3.2 (*left panels*) and by RHS97 (*right panels*). The number of clusters used to compute each relation is reported, together with the standard deviations of the data. In order to compute the scatter in an homogeneous way, only clusters in common with the RHS97 list have been considered in the left-panel plots.

the data with respect to the best-fit relation under the same assumptions, only clusters in common between our sample and RHS97 have been used. As can be see from the comparisons between each couple of panels the results are fully compatible both in terms of fit relations and data-scatter.

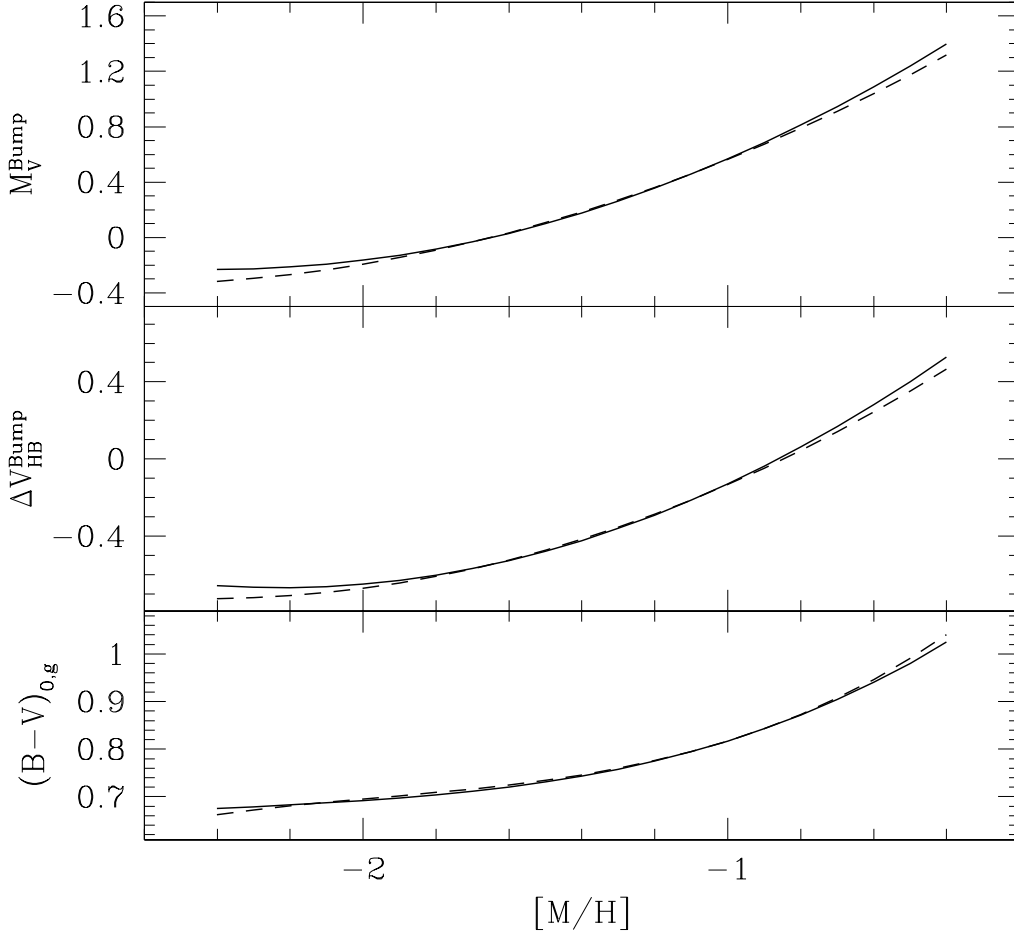


Fig. 23.— $(B - V)_{0,g}$, ΔV_{HB}^{Bump} and M_V^{Bump} as a function of the global metallicity, computed adopting the α enhancement-relation plotted in Figure 1a (*solid lines*); and adopting the α enhancement scenario proposed by Carney (1996) plotted in Figure 1b (*dashed lines*). As can be seen, the two different assumptions have a very small effect on the derived relations.

(ii) In panel (a) of Figure 2 we plotted the α -element enhancing relation adopted to compute the global metallicity listed in column 4 of Table 1. However, as discussed in Section 3.4 the trend of the $[\alpha/Fe]$ as a function of $[Fe/H]$, at least for GGCs, is still very uncertain especially in the high-metallicity domain. For this reason we show the effects of different assumptions in the α -enhancing relation on our results. We adopted the scenario proposed by Carney (1996) and plotted in Figure 2b. Even in this case for sake of example in Figure 23 we plotted three relations

obtained in the previous Sections (respectively for $(B - V)_{0,g}$, ΔV_{HB}^{Bump} and M_V^{Bump}) as a function of the global metallicity computed adopting the two different scenarios. In particular: *solid lines* are the best-fit relation obtained using global metallicity listed in Table 2, while *dashed lines* are computed adopting the Carney (1996) scenario. As can be seen, only a small effect is visible at the extreme ends of the relations, as expected, since the assumption of the Carney (1996) scenario only slightly increases (on average by 0.07 dex, the maximum being 0.13 dex) the global metallicity for metal rich (with $[Fe/H]_{CG97} < -1$) clusters (13 in our sample).

In summary, we can reasonably conclude that the relations derived in this paper are little affected by the assumptions we adopted for the metallicity.

10. CONCLUSIONS AND FUTURE PROSPECTS

A careful revision of all the best available CMDs for the Post-Main Sequence branches (RGB, HB, AGB) of GGCs has allowed to build a wide data-set. A variety of observables quantitatively describing the main properties of the considered branches as far as the location and the basic features in the CMDs were measured: the various quantities obtained via an homogeneous procedure applied to each individual CMD have been examined with varying the cluster metallicity, taking also into account the effects of α -enhancements and compared with the predictions of theoretical models. Very schematically this comparison has shown a substantial agreement between observations and theoretical predictions, with a significant improvement with respect to any similar previous study. The basic items which contribute to this result are: (i) the availability of a carefully tested wide sample of clusters (61); (ii) the adoption of an innovative, homogeneous procedure to estimate the ZAHB level; (iii) the adoption of new metallicity scales; (iv) the comparison with up-dated, self-consistent models.

Further significant improvements in the analysis could be eventually done as soon as new data for other clusters will be available and in particular when more accurate estimate on the global metal content ($[Fe/H]$ and α -elements) of GGC stars will be obtained via high resolution spectroscopy and new more accurate absolute distance moduli will be measured via alternative complementary methods.

11. Acknowledgements

We warmly thank a dear friend (Bob Rood) for a careful reading of the manuscript. The financial support of the “Ministero della Università e della Ricerca Scientifica e Tecnologica (MURST)” to the project *Stellar Evolution* is kindly acknowledged. FRF acknowledges the ESO visitor program for its hospitality.

REFERENCES

- Alexander, D.R., Fergusson, J.W., 1994, ApJ, 437, 879
 Alongi, M., Bertelli, G., Bressan, A., Chiosi, C., 1991, A&A, 244, 95
 Armandroff, T.E., Zinn, R., 1988, AJ, 96, 92.

- Beaudet, G., Petrosian, V., Salpeter, E.E., 1967, ApJ 150, 979
- Bergbusch, P.A. 1993, AJ, 106, 1024.
- Bergbusch, P.A. 1996, AJ, 112, 1061.
- Bessell, M.S., Castelli, F., Plez, B., 1998a, A&A 333, 231
- Bessell, M.S., Castelli, F., Plez, B., 1998b, A&A 337, 321
- Bono, G., Castelli, V., Degl'Innocenti, S., Pulone, L., 1995, A&A, 297, 115
- Bordoni, M.A., 1995, Master Thesis, unpublished
- Borissova, J., Catelan, M., Spassova, N., Sweigart, A.V., 1997, AJ, 113, 692
- Borissova, J., Catelan, M., Ferraro, F.R., Spassova, N., Buonanno, R., Iannicola, G., Richtler, T., Sweigart, A.V., 1999, A&A, 343, 813
- Brocato, E., Castellani, V., Ripepi, V. 1995, AJ, 109, 1670.
- Brocato, E., Buonanno, R., Malakhova, Y., Piersimoni, A.M. 1996, A&A, 311,778.
- Brocato, E., Castellani, V., Scotti, G.A., Saviane, I., Piotto, G., Ferraro, F.R., 1998, A&A, 335, 929.
- Buonanno, R., Corsi, C.E., Fusi Pecci, F., Alcaino, G., Liller, W. 1984, A&ASS, 57, 75.
- Buonanno, R., Corsi, C.E., Fusi Pecci, F., 1981, MNRAS, 196, 435
- Buonanno, R., Corsi, C.E., Fusi Pecci, F., 1985, A&A, 145, 97
- Buonanno, R., Caloi, V., Castellani, V., Corsi, C., Fusi Pecci, F., Gratton, R. 1986, A&ASS, 66, 79.
- Buonanno, R., Corsi, C.E., Ferraro, I., Fusi Pecci, F. 1987, A&ASS, 67, 327.
- Buonanno, R., Corsi, C.E., Fusi Pecci, F., 1989, A&A, 216, 80
- Buonanno, R., Fusi Pecci, F., Cappellaro, E., Ortolani, S., Richtler, T., Geyer, E.H. 1991, AJ, 102, 1005.
- Buonanno, R., Corsi, C.E., Fusi Pecci, F., Fahlman, G.G., Richer, H.B. 1993, AJ, 105, 184.
- Buonanno, R., Corsi, C.E., Buzzoni, A., Cacciari, C., Ferraro, F.R., Fusi Pecci, F. 1994, A&A, 290,69
- Buonanno, R., Corsi, C.E., Fusi Pecci, F., Richer, H.B., Fahlman, G.G. 1995a, AJ, 109, 650.
- Buonanno, R., Corsi, C.E., Pulone, L., Fusi Pecci, F., Richer, H.B., Fahlman, G.G. 1995b, AJ, 109, 663.
- Buonanno, R., Corsi, C.E., Bellazzini, M., Ferraro, F.R., Fusi Pecci 1997, AJ, 113, 706.
- Buzzoni, A., Fusi Pecci, F., Buonanno, R., Corsi, C.E. 1983, A&A, 128, 94.
- Cacciari, C., 1998 in ASP Conf. Ser. , Harmonizing Cosmic Distance Scales in a Post-Hipparcos Era, eds. Egret D. & Heck A. (San Francisco: ASP), (in press).
- Caputo, F., Chieffi, A., Tornambe, A., Castellani, V., Pulone, L., 1989, ApJ, 340, 241.
- Carney, B.W., 1996, PASP, 108, 900.
- Carney, B.W., Fullton, L.K., Trammell, S.R., 1991, AJ, 101, 1699
- Carney, B.W., Storm, J., Jones, R.V. 1992, ApJ, 386, 663.
- Carretta, E., Gratton, R.G. 1997, A&ASS, 121, 95.
- Carretta, E., Bragaglia, A. 1998, A&A, 329, 937.
- Carretta, E., Gratton, R.G., Clementini, G., Fusi Pecci, F., 1999, astro-ph9902086 (C99)
- Cassisi, S., Salaris, M., 1997, MNRAS, 285, 593.
- Castellani, V. & Tornambe', A., 1977, A&A, 61, 427.
- Castellani, V., Chieffi, A., Tornambe, A., Pulone, L., 1985, ApJ, 294, 31.
- Castellani, V., Chieffi, A., Pulone, L., 1989, ApJ, 344, 239.
- Castellani, V., Chieffi, A., Pulone, L., 1991, ApJS, 76, 911.
- Caughlan, G.R., Fowler, W.A., Harris, M.J., Zimmerman, B.A., 1985, Atomic Data and Nuclear Data Tables,

32, 197.

- Caughlan, G.R., Fowler, W.A., 1988, *Atomic Data and Nuclear Data Tables*, 40, 283.
- Chaboyer, B., Demarque, P., Sarajedini, A., 1996, *ApJ*, 459, 558
- Chieffi, A., Straniero, O., *ApJS*, 71, 47.
- Chieffi, A., Limongi, M., Straniero, O., 1998, (in preparation) (CLS98).
- Christian, C.A., Heasley, J.N. 1988, *AJ*, 95, 1422.
- Cohen, J.G., 1983, *ApJ*, 270, 654.
- Covino, S., Ortolani, S. 1997, *A&A*, 318, 40.
- Cudworth, K.M. 1988, *AJ*, 96, 105.
- Cudworth, K.M. 1995, *AJ*, 90, 65.
- Desidera, S., 1996, Master Thesis
- Dicus, D.A., Kolb, E.W., Schramm, D.N., Tubbs, D.L., 1976, *ApJ*, 210, 481
- Djorgovski, G.S., 1993, in *ASP Conf. Ser. 50, Structure and dynamics of Globular Clusters*, ed. Djorgovski, G.S. & Meylan, G., (San Francisco: ASP), 373
- Dorman, B., Rood, R.T., 1993, *ApJ*, 409, 387.
- Edvarsson, B., Andersen, J., Gustafsson, B., Lambert, D.L., Nissen, P.E., Tomkin, J., *A&A*, 275, 101.
- Ferraro, F.R. 1992, *MSAIt*, 63, 491.
- Ferraro, F.R., Clementini, G., Fusi Pecci, F., Buonanno, R., Alcaino, G. 1990, *A&ASS*, 84, 59.
- Ferraro, F.R., Clementini, G., Fusi Pecci, F., Buonanno, R., 1991, *MNRAS*, 252, 357.
- Ferraro, F.R., Clementini, G., Fusi Pecci, F., Sortino, R., Buonanno, R. 1992, *MNRAS*, 256, 391.
- Ferraro, F.R., Fusi Pecci, F., Buonanno, R. 1992, *MNRAS*, 256, 376.
- Ferraro, F.R., Clementini, G., Fusi Pecci, F., Vitiello, E., Buonanno, R. 1993a, *MNRAS*, 264, 273.
- Ferraro, F.R., Fusi Pecci, F., Cacciari, C., Corsi, C.E., Buonanno, R., Fahlmann, G.G., Richer, H.B., 1993b, *AJ*, 106, 2324.
- Ferraro, F.R., Fusi Pecci, F., Guarnieri, M.D., Moneti, A., Origlia, L., Testa, V. 1994, *MNRAS*, 266, 829.
- Ferraro, F.R., Fusi Pecci, F., Bellazzini, M. 1995, *A&A*, 294, 80.
- Ferraro, F.R., Carretta, E., Corsi, C.E., Fusi Pecci, F., Cacciari, C., Buonanno, R., Paltrinieri, B., Hamilton, D., 1997a, *A&A*, 320, 757.
- Ferraro, F.R., Paltrinieri, B., Fusi Pecci, F., Cacciari, C., Dorman, B., Rood, R.T., 1997b, *ApJ*, 484, L145.
- Ferraro, F.R., Paltrinieri, B., Fusi Pecci, F., Cacciari, C., Dorman, B., Rood, R.T., Buonanno, R., Corsi, C.E., Burgarella, D., Laget, L., 1997c, *A&A*, 324, 915.
- Ferraro, F.R., Paltrinieri, B., Fusi Pecci F., Rood, R.T., Dorman, B., 1998a, *ApJ*, 500, 311.
- Ferraro, F.R., Paltrinieri, B., Rood, R.T., Dorman, B., 1998b, *ApJ*, (in press)
- Ferraro, I., Ferraro, F.R., Fusi Pecci, F., Corsi, C.E., Buonanno R. 1995, *MNRAS*, 275, 1057.
- Fusi Pecci, F., Ferraro, F.R., Crocker, D., Rood, R.T., Buonanno, R., 1990, *A&A*, 238, 95 (F90).
- Fusi Pecci, F., Ferraro, F.R., Corsi, C.E., Cacciari, C., Buonanno, 1992 *AJ*, 104, 1831.
- Fusi Pecci, F., Ferraro, F.R., Bellazzini, M., Djorgovski, S., Piotto, G., Buonanno, R. 1993, *AJ*, 105, 1145.
- Gratton, R., Carretta, E., Matteucci, F., Sneden, C., 1996, in *ASP Conf. Ser. 92, The formation of the Galactic Halo... Inside and Out*, ed. Morrison H. & Sarajedini, A., (San Francisco: ASP), 307
- Gratton, R., Fusi Pecci, F., Carretta, E., Clementini, G., Corsi, C.E., Lattanzi, M., 1997, *ApJ*, 491, 749.
- Harris, W.E. 1982, *ApJSS*, 50, 573.

- Harris, W.E. 1996, *AJ*, 112, 1487.
- Harris, W.E., Racine, R., De Roux, J, 1976, *ApJSS*, 31, 13.
- Hartwick F. D. A., 1968, *ApJ* 154, 475
- Hesser, J.E., Harris, W.E., Vandenberg, Allwright, J.W., Shott, P., Stetson, P.B., 1987, *PASP*, 99, 739.
- Iben, I.Jr., 1968, *Nature*, 220, 143.
- Iglesias, C.A., Rogers, F.J., Wilson, B.G., 1992, *ApJ*, 397, 717
- Itoh, N., Mitake, S., Iyetomi, H., Ichimaru, S., 1983, *ApJ*, 275, 858
- Kalusny, J., 1997, *A&ASS*, 122, 1.
- King, C.R., Da Costa, G.S., Demarque, P, 1985, *ApJ*, 299, 674
- Janes, K.A., & Heasley J.N., 1991, *AJ*, 101, 2097
- Lee, Y.-W., Demarque, P., Zinn, R., 1990, *ApJ*, 350, 155.
- Lee, S.W. 1977, *A&AS*, 28, 409.
- Magain, P., 1989, *A&A*, 209, 211
- Momany, Y. 1996, Master Thesis, unpublished.
- Montegriffo, P., Ferraro, F.R., Fusi Pecci, F, Origlia, L. 1995, *MNRAS*, 276, 739.
- Munakata, H., Kohyama, Y., Itoh, N., 1985, *ApJ*, 296, 197
- Nissen, P.E., Gustafsson, B., Edvardsson, B., Gilmore, G., 1994, *A&A*, 285, 440
- Ortolani, S., Gratton, R. 1990, *A&ASS*, 82, 71.
- Ortolani, S., Barbuy, B., Bica, E. 1994a, *A&ASS*, 108, 653.
- Ortolani, S., Bica, E., Barbuy, B. 1994b, *A&A*, 286, 444.
- Ortolani, S., Renzini, A., Gilmozzi, R., Marconi, G., Barbuy, B., Bica, E. 1995, *Nature*, 377, 701.
- Paltrinieri, B., Ferraro, F.R., Fusi Pecci, F., Carretta, E., 1998, *MNRAS*, 293, 434
- Pike, C.D., 1976, *MNRAS*, 177, 257.
- Pulone, L., 1992, *MSAIt*, 63, 485.
- Reid, I.N., 1997, *AJ*, 114, 161
- Reid, I.N., 1998, *AJ*, 115, 204
- Renzini, A., Fusi Pecci, F. 1998, *ARA&A*, 26, 199
- Renzini, A., Bragaglia, A., Ferraro, F.R., Gilmozzi R., Ortolani S., Holberg J.B., Wesemael F., Bohlin R.C., 1996, *ApJ*, 465, L23.
- Rood, R.T, 1973, *ApJ*, 184, 815
- Rood, R.T, Whitney, J.H., D'Cruz, N.L., 1997, in *Advances in Stellar Evolution* ed. R. T. Rood & A. Renzini (Cambridge: Cambridge U. Press), 74.
- Rutledge, G.A., Hesser, J.E., Stetson, P.B., 1997, *PASP*, 109, 907 (RHS97)
- Salaris, M., Chieffi, A., Straniero, O., 1993, *ApJ*, 414, 580.
- Salaris, M., Cassisi, S., 1996, *A&A*, 305, 858.
- Samus, N., Ipatov, A., Smirnov, O., Kravtsov, V., Alcaino, G., Liller, W., Alvarado, F. 1995, *A&ASS*, 112, 439.
- Sandage, A.R., Walker, M.F. 1955, *AJ*, 60, 230.
- Sandage A. R., Smith L. L., 1966, *ApJ* 144, 886
- Sandage A. R., Wallerstein G., 1960, *ApJ* 131, 598
- Sarajedini, A. 1994a, *PASP*, 106, 404.

- Sarajedini, A., 1994b, AJ 107, 618
- Sarajedini, A., Norris, J.E., 1994, ApJS, 93, 161 (SN94)
- Sarajedini, A., Milone, A.A.E. 1995, AJ, 109, 269.
- Sarajedini, A., Forrester, W.L. 1995, AJ, 109, 1112.
- Sarajedini A., Layden A., 1997, AJ 113, 264
- Straniero, O., 1988, A&AS, 76, 157.
- Straniero, O., Chieffi, A., 1991, ApJS, 76, 525
- Straniero, O., Chieffi, A., Salaris, M., 1992, MSAIt, 63, 315
- Straniero, O., Chieffi, A., Limongi, M., 1997, ApJ, 490, 425 (SCL97).
- Thomas, H.C., 1967, Z. Ap, 67, 420
- VandenBerg, D.A., Stetson, P.B., Bolte, M., 1996, ARA&A, 34, 461
- Walker, A.R. 1990, AJ, 100, 1532.
- Walker, A.R. 1992a, AJ, 104, 1395.
- Walker, A.R. 1992b, PASP, 104, 1063.
- Walker, A.R. 1994, AJ, 108, 555.
- Whitney, J.H., Rood, R.T., O'Connell, R.W., D'Cruz, N.L., Dorman, B., Landsman, W.B., Bohlin, R.C., Roberts, M.S., Smith, A.,M., Stecher, T.P., 1998, ApJ, 495, 284.
- Zinn, R.J. 1980, ApJS, 42, 19.
- Zinn, R.J. 1985, ApJ, 293, 424 (Z85)
- Zinn, R.J., West, M.J. 1984, ApJS, 55, 45.
- Zhao, G., Magain, P., 1990, A&A, 238, 242